ISSN 2708-6437(Online)
2708-6429(Print)

Journal of Engineering Advancements

Editor-in-Chief:
Prof. Dr. Mohammad Mashud

Volume 06 Issue 01

SciEn

Published by:
SciEn Publishing Group

Journal of Engineering Advancements
Apt. # 6 C-D, House # 191
Road # 12/A, Dhanmondi R/A
Dhaka-1209, Bangladesh
Email: jea@scienpg.com Website: www.scienpg.com/jea/

SciEn
Published in: March 2025
Published by: SciEn Publishing Group
Price: Each Issue BDT 200.00 (US$ 15) **ISSN:** 2708-6437 (Online) 2708-6429 (Print)

Journal of Engineering Advancements
Apt. # 6 C-D, House # 191
Road # 12/A, Dhanmondi R/A
Dhaka-1209, Bangladesh
Email: jea@scienpg.com Website: www.scienpg.com/jea/

Journal of Engineering Advancements

Volume 06, Issue 01 March 2025

CONTENTS

Original Articles

Journal of Engineering Advancements

Published by: SciEn Publishing Group

Apt. # 6 C-D, House # 191, Road # 12/A
Dhanmondi, Dhaka-1209, Bangladesh
Email Address: jea@scienpg.com

www.scienpg.com/jea/

This page is left intentionally blank

SciEn
Journal of Engineering Advancements Vol. 06(01) 2025, pp 1-10 https://doi.org/10.38032/jea.2025.01.001

An Experimental Study on Mechanical Properties of Stir Casted Hybrid Al Metal Matrix Composite Reinforced with Al_2O_3 and TiO_2

Md. Imtiaj Hossain, Minhaz Ahmed, Tafsirul Hassan*

Department of Mechanical Engineering, Chittagong University of Engineering & Technology, Chattogram-4349, Bangladesh

Received: October 14, 2024, Revised: December 20, 2024, Accepted: January 31, 2025, Available Online: March 04, 2025

ABSTRACT

This study investigates the impact of incorporating aluminum oxide (Al_2O_3) and titanium dioxide (TiO_2) into an aluminum matrix. The primary objectives of this research were to create composite materials with a high strength-to-weight ratio and to assess their mechanical properties. The experiment involved the homogenous dispersion of 99.9% pure aluminum powder with Al_2O_3 and TiO_2 reinforcements. Three samples were produced by the stir casting method, utilizing finely ground aluminum powder mixed with an equal proportion of Al_2O_3 and TiO_2 (2.5% Al_2O_3 + 2.5% TiO_2, 5% Al_2O_3 + 5% TiO_2, 7.5% Al_2O_3 + 7.5% TiO_2). The morphological distribution of reinforcements was determined through structural analysis utilizing a scanning electron microscope (SEM). Tests were undertaken to examine the mechanical qualities of hardness, tensile strength and impact strength. The addition of reinforcement to the aluminum matrix leads to a reduction in hardness. The highest tensile strength observed in the sample reinforced with a combination of 5% Al_2O_3 and 5% TiO_2. Conversely, the incorporation of reinforcements was observed to enhance the impact strength. The current hybrid aluminum metal matrix composite is considered valuable for diverse engineering applications that require a high strength-to-weight ratio.

Keywords: Metal matrix composite, Aluminum, Stir casting, Microstructure, Mechanical properties.

1 Introduction

Metal matrix composites (MMCs) are advanced materials made of a metal matrix reinforced with organic, ceramic and metallic components. MMCs are materials with better mechanical properties than their components. Currently, MMCs are available for use in Engineering applications in a range of forms. Most sectors, including electronics, defense, automotive and aviation, employ MMCs extensively. The discovery of MMCs has opened up a new line of inquiry into material science and engineering. Combining two or more insoluble elements that collectively possess better properties than any of the parts alone yields a composite material. When compared to traditional materials like steel, composite materials are lighter and more robust [1]. Two phases of composite materials are the matrix and the reinforcing phase. The constituents of composite materials are called reinforcements, and they typically consist of a matrix, a continuous phase and one or more discontinuous phases. The matrix keeps the reinforcement in place to achieve the desired shape, even if it enhances the matrix's overall properties [2]. Aluminum matrix composites (AMCs), are highly suited materials for many applications due to their robust physical and mechanical properties. Utilizing reinforcements improves the stiffness and particular durability, wear, creep, and fatigue properties of the metallic matrix compared to conventional Engineering materials [3]. Aluminum and its alloys have drawn the most interest as the base metal for metal matrix composites. Aluminum MMCs are frequently used in automobiles, aerospace, and several other industries. When operating at the designated temperature, the reinforcements must be both stable and non-reactive. Silicon carbide and aluminum oxide are the most often used reinforcing materials [4].

Al6061-Al_2O_3 composites containing 5 wt.% tiny Al_2O_3 particles were prepared by V. Balaraj et al. [5], and scanning electron microscopy (SEM) verified that the Al_2O_3 particles were evenly distributed throughout the matrix. Comparing the synthetic composites to the unreinforced Al6061 alloy, the former showed improved hardness, tensile strength, and impact strength. SEM investigation revealed little porosity in the matrix, although localized strain caused tiny voids to appear on the composites' fracture surfaces. Sajjadi et al. [6] employed a three-step mixing technique to fabricate materials containing 5 wt.% micron-sized and 3 wt.% nano-sized Al_2O_3 reinforcement. This was done to enhance the wetting and dispersion properties inside an aluminum alloy matrix. As the wt.% of Al_2O_3 rose, the hardness, porosity, and compressive strength also increased. Krishna et al. [7] have attempted to prepare and compare the mechanical properties of Al6061-SiC and Al6061-SiC/Graphite hybrid composites using the stir casting method. The composites have undergone microstructural investigations to describe them, with reinforcement varying between 5 and 15 wt.%. Although actual densities were lower than predicted theoretically, uniform particle dispersion with some clumping and higher tensile strength was found. Saravanan et al. [8] have explored the reinforcement of AlSi10Mg alloy with rice husk ash (RHA) to develop cost-effective metal matrix composites. It has been demonstrated that adding RHA to the composite at different weight percentages (3%, 6%, 9%, and 12%) improves its mechanical characteristics. SEM analysis has verified that the RHA particles are distributed evenly. Increased RHA content has been shown to improve tensile strength, compressive strength, and hardness, indicating its potential as a reinforcing agent. A study conducted by Ahmadifard et al. [9] focused on the manufacturing and analysis of a hybrid surface nanocomposite consisting of A5083, Al_2O_3 and TiO_2. This composite was produced using friction stir processing (FSP). The findings indicated that a combination of 25% Al_2O_3 and 75% TiO_2 yielded

*Corresponding Author Email Address: minhaz@cuet.ac.bd Published by: SciEn Publishing Group

materials with the highest tensile strength of 350 MPa and a microhardness rating of 158 HV. Utilizing in-situ Al-based MMCs generated from the Al–10 wt.% TiO_2 and Al–10 wt.% TiO_2-1.5 wt.% C systems. Peng Yu et al. [10] carried out another series of tests utilizing hot isostatic pressing (HIP) at 1000 °C and 100 MPa. Carbon's (C) inclusion aided in the intermetallic plates' elimination. The Al–10 wt.% TiO_2-1.5 wt.% C composite showed considerably better strength and strain-at-break compared to its Al–10 wt.% TiO_2 counterpart, according to three-point bending tests. The stir casting technique was effectively employed to fabricate a MMC reinforced with aluminum and a hybrid of Al_2O_3 and carbon. The results stated that there was no chemical interaction between the reinforcing components, carbon, Al_2O_3, and the aluminum matrix. The composite density decreased as the reinforcement concentration increased, reaching a minimum density of 2.04 gm/cm^3 in the AlAlOC05 specimen. The addition of carbon to the aluminum matrix resulted in a decrease in density, making it suitable for lightweight applications. According to Bandil et al. [11], the SEM microstructure investigation showed that SiC and Si alloying element particles are evenly distributed throughout the Al matrix. The reinforcing particles and matrix material did not interact, according to EDX analysis, while fabrication-related ambient oxygen trapping led to the appearance of weak oxide peaks. The density decreased as the amount of SiC in the Al matrix composites increased. The composites' hardness increased with the addition of SiC particles, reaching its maximum hardness at 15% reinforcement [12]. MMCs were characterized by Lokesh et al. using an Al6063 matrix to which different quantities of Cu and TiO_2 particles were added. With an increase in the weight percentage of Cu reinforcement, there was a little elevation in the hardness of the composites. However, when the weight percentage of reinforcement increased, the ductility of the composites decreased [13].

Muna and Jabbar [14] studied the Al-12 wt.% Si matrix composites reinforced with a hybrid addition of 2, 4 and 6 wt.% nanoparticles of Al_2O_3 and TiO_2 that exhibit dry sliding wear behavior. With varied loads and sliding periods, dry sliding wear experiments were performed and the worn surface micrographs were examined using SEM to examine wear traces and debris morphology. According to the findings, when compared to other nanocomposites, the nanocomposite containing 6 wt.% (Al_2O_3 + TiO_2) nanoparticles had the maximum hardness. Furthermore, the nanocomposites demonstrated a lower wear rate, indicating improved wear resistance compared to the base alloy under similar conditions. Naseem et al. [15] studied wear behavior, Vickers hardness, and wear data optimization for hybrid MMCs made of pure aluminum and Al-Al_2O_3-TiO_2. In the Al-Al_2O_3-TiO_2 hybrid composite, Vickers hardness rose as reinforcement proportion increased. The findings of the Analysis of Variance (ANOVA) showed that the wear rate of the hybrid composites was affected differently by both load and reinforcement. Adhesive wear predominated at lower reinforcement percentages, but abrasive wear was more common at higher reinforcement percentages, according to SEM inspection of the worn surfaces. El Mahallawi et al. [16] employed rheo-casting and included Al_2O_3/TiO_2 nanoparticles into the Al-Si slurry to produce hypereutectic aluminum-silicon samples (A390). The inclusion of nanoparticles and mechanical stirring resulted in an increase in the microhardness, hardness, and wear resistance of the A390 alloys. The addition of nanoparticles resulted in a reduction in the average size of the Si particles and an increase in hardness. The study demonstrated that the incorporation of Al_2O_3/TiO_2 nanoparticles into hypereutectic aluminum alloys yielded favorable effects. Hamid et al. [17] studied cast in situ Al(Ti)-Al_2O_3-TiO_2 composites, which are formed by dispersing TiO_2 particles in molten aluminum. Different sliding speeds under constant load and normal loads were used for wear experiments. Under identical sliding circumstances, cast in situ composites had considerably lower cumulative volume reduction and wear rates than cast commercial aluminum or cast unreinforced Al-Ti base alloys. Porosity reduced wear resistance, sometimes overshadowing reinforcing particles. Zhang et al. [18] conducted another experiment employing a mix of Al and TiO_2 powders in multiple pass friction stir processing (FSP) to manufacture in situ Al composites. The experiment was guided by thermodynamic analysis. The in-situ nanocomposites exhibited a reasonable equilibrium between strength and ductility during tensile testing and demonstrated a significant inclination towards work hardening. By using SEM, Shuvho et al. [19] exposed plowing, micro-wear, micro-cracks, fractures, voids, and particle pull-out on the surface of the Al_2O_3, SiC, and TiO_2 MMC. According to the topographical and textural analysis results, the Al6063 matrix has an evenly distributed dispersion of Al_2O_3, SiC, and TiO_2. This study demonstrates that the mechanical characteristics of the alloy, such as its hardness, tensile strength, and yield strength, are greater than those of pure Al6063 metals and increase with increasing SiC. Also, various functional groups were identified, such as O-H, C-H, CN, and -OH. El-Mahallawi et al. [20] conducted a study to explore a novel method of enhancing the characteristics of cast aluminum alloys. The analysis included introducing nanoparticles of ZrO_2, TiO_2, and Al_2O_3 into the A356 aluminum cast alloy. Analysis of the microstructure and fracture surface showed nanoparticles' existence, leading to grain morphology alterations and improved mechanical characteristics, including strength, elongation, and hardness. The incorporation of nanoparticles did not provide a substantial enhancement in the wear resistance of the hypo-eutectic A356 alloy and increasing percentages of nanoparticles resulted in a decline in performance.

Li et al. [21] effectively used FSP to create surface composites of copper matrix supplemented with Al_2O_3/TiO_2 particles. The thickness of the composite layer after undergoing three passes of processing was about 2200 µm. The addition of Al_2O_3/TiO_2 particles enhanced the hardness and thermal stability of the composites and the fracture analysis demonstrated a combination of fracture patterns, with the particles being effectively enveloped by the substrate. Ni-based alloy composite coatings were produced using the plasma spray process, using nanostructured Al_2O_3-40%TiO_2 ceramic particles as reinforcement. The findings indicate that the composite coatings mostly include γ-Ni, α-Al_2O_3, γ-Al_2O_3, and rutile-TiO_2. These coatings demonstrate reduced friction coefficients and wear losses compared to Ni-based alloy coatings at various loads and speeds. Due to the escalating contact stress over the elastic threshold, it undergoes a transition to abrasive wear, micro-brittle fracture wear, and multi-plastic deformation wear. Higher velocities lead to a 13.8% drop in the average friction coefficient and a 36.5% reduction in wear loss compared to the coating made of Ni-based alloy [22]. Nayak et al. [23] highlighted the significance of using nanofillers (Al_2O_3 and TiO_2) in glass fiber-reinforced polymer composites to observe the effect on the variation of interlaminar shear strength (ILSS). The research used SEM to examine the fracture surfaces and assess the influence of crosshead speed (CS) on the testing process.

Introducing several nanofillers resulted in higher values of ILSS and shear strain when compared to the control composites.

Jamwal et al. [24] examined the influence of SiC-graphite reinforcement on the properties of pure copper, which was fabricated using the stir-casting technique. The microstructure analysis showed a uniform distribution of SiC-graphite throughout the material. Graphite decreased hardness and density, which makes it well-suited for lightweight applications. The incorporation of SiC-graphite improves the wear resistance, exhibiting the most advantageous corrosion resistance. Paulraj et al. [25] reinforced aluminum with varying percentages of nano TiO_2, micro SiC, and B_4C respectively using a stir casting process. During manufacturing, the reinforcements were swirling at 600 rpm and heated to 750°C. Tensile strength increased from 0.5% to 1% upon the addition of TiO_2, however, elongation and impact strength decreased as the volume (%) of nano TiO_2 increased. Wear, abrasion, and friction resistance were all enhanced by combining 1% TiO_2, 10% SiC, and 10% B_4C. Toughness was increased and mass loss was decreased because of the high density. Kanthavel et al. [26] conducted a study on the three kinds of Aluminum hybrid composites that were created using powder metallurgy. The wear and friction characteristics of the three examined combinations, namely Al + 5% Al_2O_3, Al + 5% Al_2O_3 + 5% MoS_2 and Al + 5% Al_2O_3 + 10% MoS_2, were shown to be dependent on the proportion of MoS_2. The hybrid composite consisting of Al + 5% Al_2O_3 + 5% MoS_2 exhibits the lowest level of wear. The investigation indicates that including an additional 10% MoS_2 into the composite does not contribute to enhancing its tribological characteristics. Luo et al. [27] studied the alteration of KH560, an epoxy-functional silane, after hydrothermally synthesizing spherical Al_2O_3/TiO_2 nanocomposites. The average diameter of the modified nanoparticles was 75 nm, and they exhibited good dispersion stability in lubricating oil. Through four-ball and thrust-ring testing, it was shown that the addition of modified Al_2O_3/TiO_2 nanocomposites at an optimal concentration of 0.1 wt.% dramatically reduced friction coefficients and increased anti-wear performance. The nanocomposites converted sliding friction into rolling friction by forming a shielding covering on the rubbing surfaces during friction. Ylma et al. [28] produced Al_2O_3-TiO_2 plasma sprayed coatings of different compositions on an AISI 304L stainless steel substrate. Investigations were conducted to determine how the addition of TiO_2 affected the coatings. It was evident from the traditional evaluation of the experimental results that a higher TiO_2 concentration reduced microhardness values and enhanced fracture toughness. The microhardness of the alumina coating was dramatically reduced by the addition of TiO_2, which increased toughness. Aluminum, magnesium, and graphite have lower densities than copper, as shown by Oddone et al. [29]. They obtain four times greater heat conductivity than copper because of their low density. An Aluminum-3003 alloy metal matrix, reinforced with single-walled carbon nanotubes (CNTs) and titanium carbide (TiC), was produced using the stir casting technique. It has been observed that when the number of reinforcements increases, particles are more even. The density of composites decreases as a result of the volatile nature of the reinforcing particles. Reinforcement determines composite hardness and composites wear less as load lowers and reinforcing rises [30].

It seems that not enough research has been done on the microstructure analysis of hybrid AMMCs. There hasn't been enough thorough research done on the mechanical characterization of hybrid AMMCs and the effects of various reinforcing arrangements, manufacturing techniques on the mechanical characteristics of hybrid AMMCs. This study has been conducted to close the information gap about the mechanical properties of a stir-casted hybrid AMMC reinforced with Al_2O_3 and TiO_2. This research aims to examine the structural and mechanical characteristics of a hybrid composite material. A hybrid composite, consisting of Al_2O_3 and TiO_2, has been fabricated via stir casting. This involves analyzing many aspects of the final composite material, such as its microstructure, hardness, impact strength, and tensile strength. To further enhance this investigation, modern manufacturing techniques like as infiltration, plasma sintering, hot pressing, and powder metallurgy may be used.

2 Materials and Method

2.1 Stir Casting Method

The first stage in producing an Al-Al_2O_3-TiO_2 matrix by the stir casting method entails obtaining high-purity sample powders of Al, Al_2O_3, and TiO_2 from an accredited vendor. The reinforcements utilized consist of Al_2O_3 powder with a purity of 96% and TiO_2 powder with a purity of 99%. The stir casting system used a silicon carbide stirrer, a graphite crucible, an electrical furnace, a temperature controller, and a cylindrical die composed of high chrome high carbon steel. To fabricate the samples, the powders are measured based on the specified wt.% chosen. Three samples with varied weight proportions have been created throughout the production process. The weights of the powders vary depending on the individual tests being performed. Al_2O_3 and TiO_2 are used as the reinforcing material, with aluminum serving as the matrix material in this case. The final specimen is prepared using a total of 600 g of powder. A quantity of 200 g has been used for each combination. In this case, 190 g of Al is combined with 5 g each of TiO_2 and Al_2O_3, resulting in a composition of 95% Al, 2.5% TiO_2, and 2.5% Al_2O_3. The remaining two combinations have been acquired in the same way. To reduce the moisture content, the crucible has spent 30 min in the electrical furnace at 510 °C. Then, to remove moisture and stop oxidation, reinforcement materials such as Al_2O_3 and TiO_2 have been put in the crucible and held within the furnace for 45 min at 540 °C. In this procedure, the Aluminum powder is not warmed to avoid the oxidation of aluminum.

To achieve the needed criteria, the Al matrix has been broken up into smaller pieces and weighed appropriately using an automated weighing scale. The Al matrix was then been added to the crucible before being put inside the furnace. The temperature of the furnace has been raised progressively to 920 °C and then held there for 30 min. The Al matrix has then melted and gradually changed into a molten state after a 30-min period. Then, the warmed reinforcements were placed in the furnace and stirred for 30 min before being heated to 940 °C for 8 min. The fusion of the matrix and reinforcing components has been successfully achieved in the furnace via the process of melting. After the particles were completely liquefied, a manual stirring method was used using a hand stirrer. A vortex was generated in the molten aluminum by rotating the stirrer for a duration of 10 min. Once the metal has been melted, it is next poured into molds to get the desired form of the specimen. The final samples have been produced after the molds solidified. Once the composites have fully hardened, further techniques such as thread cutting, taper turning, grinding and slot cutting must be performed. The tensile specimens were fabricated using thread-cutting and taper

turning techniques. Slots were added to the impact specimens. Final specimens were produced after completing all the tasks outlined in Table 1.

Table 1 Nomenclature of Al-Al_2O_3-TiO_2 hybrid composite samples.

Sample	Al (wt.%)	Al_2O_3 (wt.%)	TiO_2 (wt.%)
Sample (i)	95%	2.5%	2.5%
Sample (ii)	90%	5%	5%
Sample (iii)	85%	7.5%	7.5%

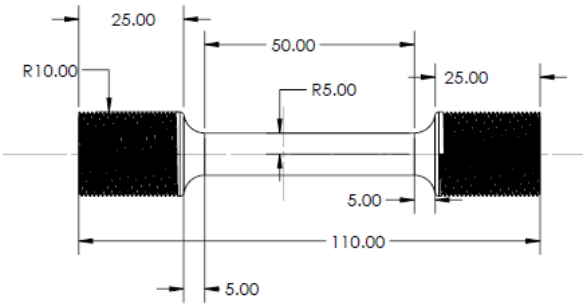

Fig. 1 Specimen for tensile test (All dimensions are in mm).

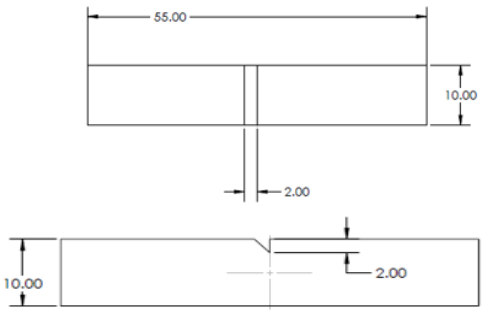

Fig. 2 Specimen for impact test (All dimensions are in mm).

(a) (b) (c)

Fig. 3 Final specimens for a) Hardness test, b) Impact test, and c) Tensile test.

(a) (b) (c)

Fig. 4 Final specimens after testing for a) Hardness test, b) Impact test, and c) Tensile test.

2.2 Characterization

The specimens were prepared using a SEM at magnifications of 500x, 1100x, 1500x, and 2000x for morphological analysis. Preparation of samples for various tests, including SEM and energy dispersive spectroscopy (EDS), involves the process of polishing. The samples were polished properly using emery paper of grades starting from 280, 360, 500, and 1000 for 20 min and after that, polishing of the samples was done with alumina gel for 20min.

To comprehend the mechanical properties of metallic materials, including their tensile strength, yield strength, and ultimate tensile strength, it is necessary to conduct tensile testing. The experimental data was collected and used to generate a stress-strain curve to analyze the tensile behavior of the specimens. A universal testing machine (UTM) was utilized to quantify the tensile strength. The dimensions of the tensile test specimen, as specified by the ASTM (American Society for Testing and Materials), are illustrated in Fig. 1. Three samples were prepared for tensile testing, and each sample was tested sequentially under identical conditions. The UTM employed was a manual device, where the applied load was controlled via a hand-operated lever or valve. The load values were displayed on a gauge, while displacement data were manually recorded from another gauge. During the test, the loading process was manually controlled by adjusting a mechanical lever to apply force to the specimens. While recording the data, there was a slight decrease in force immediately after reaching the maximum force (approximately 100 N for Sample (i)), just before the specimen fractured. From the recorded data, the maximum force (F) was used to calculate UTS, and the breaking force was used to calculate tensile strength. The cross-sectional area (A) was calculated using the initial diameter (D) of the samples. Calculations for UTS, tensile stress, and cross-sectional area were performed using the following formulas:

$$\sigma = \frac{F}{A} \tag{1}$$

$$A = \frac{\pi}{4} D^2 \tag{2}$$

The Brinell hardness tester was employed to ascertain the hardness of the composites with varying ratios. The Brinell hardness test involves applying a constant force of 10 kN for a duration of 10 s by placing a tungsten carbide ball with a diameter of 10 mm on the flat surface of a workpiece. The indentation diameter is determined by measuring the horizontal and vertical axis radii of the hole formed, and then calculating their average using a digital slide caliper. Charpy V-notch test was employed to quantify the energy absorbed by the samples before fracture. The purpose of loading the specimens into the machine was to fracture them ultimately. The impact value was promptly derived from the measurement of impact strength utilizing a digital impact tester apparatus. The dimensions of the Charpy test specimen for measuring impact strength are also depicted in Fig. 2.

3 Results and Discussions

3.1 Microstructure Analysis

3.1.1 Distribution of Reinforcements

The microstructure analysis was employed to investigate the morphological behavior of the composite material that was produced. Fig. 5 displays the SEM images of the sample (ii) consisting of 90% Al, 5% Al_2O_3, and 5% TiO_2. The images were captured at magnifications of 500x, 1100x, and 2000x, respectively. Due to its non-conductive nature, Al_2O_3 tends to form clusters in certain areas and appear white. The regions in the image showing such clustering and whiteness are Al_2O_3. On the other hand, TiO_2 has some recognizable visual traits, such as rounded shapes and bright contrast. In the SEM image, we identified and marked certain areas based on these characteristics as potential TiO_2.

The distribution of reinforcements throughout the Al matrix is found to be uniform. This guarantees that the highest possible amount of reinforcement particles in the aluminum matrix is dispersed homogeneously due to the insoluble nature of the Al_2O_3 and TiO_2 particles.

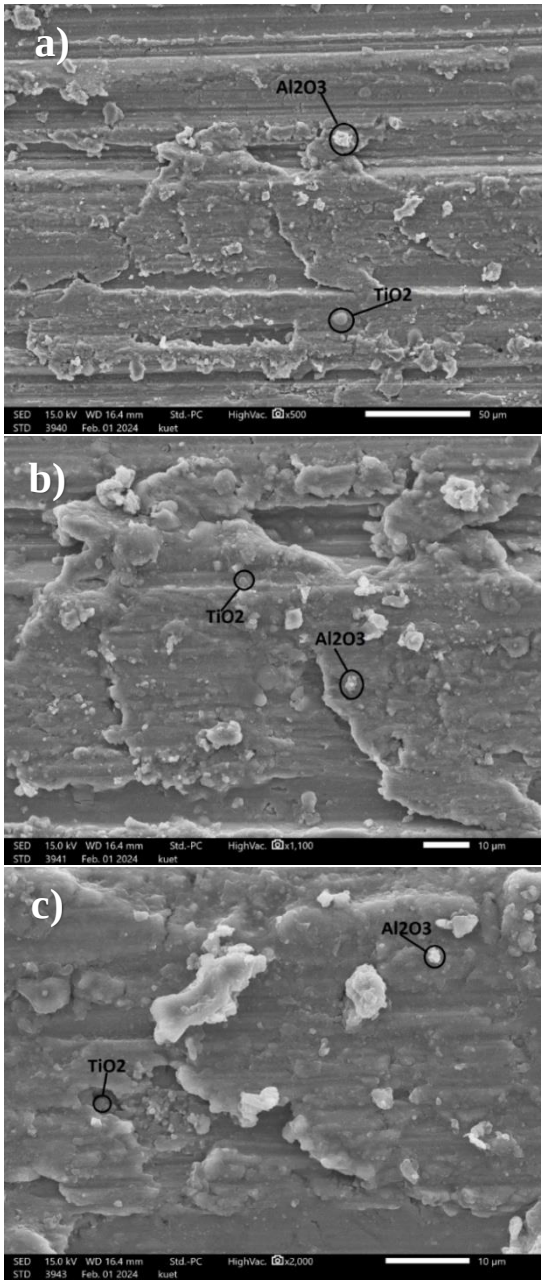

Fig. 5 SEM micrograph of sample (ii) at a) 500x magnification, b) 1100x magnification, and c) 2000x magnification.

In the stir casting process, it is clearly observed that reinforcement particles get collected during the stirring process. It is a difficult task to properly mix and distribute Al_2O_3 and TiO_2 inside the aluminum matrix. It is possible to achieve a homogeneous microstructure with reduced reinforcing concentrations. Particle agglomeration occurs during the stirring process as a result of the substantial density variations between the matrix and reinforcement phases, which make it more difficult to achieve equal distribution at higher concentrations. Also, there is a high chance of getting a non-uniform distribution of reinforcements because of an improper stirring process.

3.1.2 Grain Size Distribution

We examined the grain size distribution of sample (ii) using Image J and Origin Pro software. Fig. 6 depicts SEM micrographs of the sample at 1500x and 2000x magnifications, respectively, showcasing a uniform distribution of grains within the Al matrix.

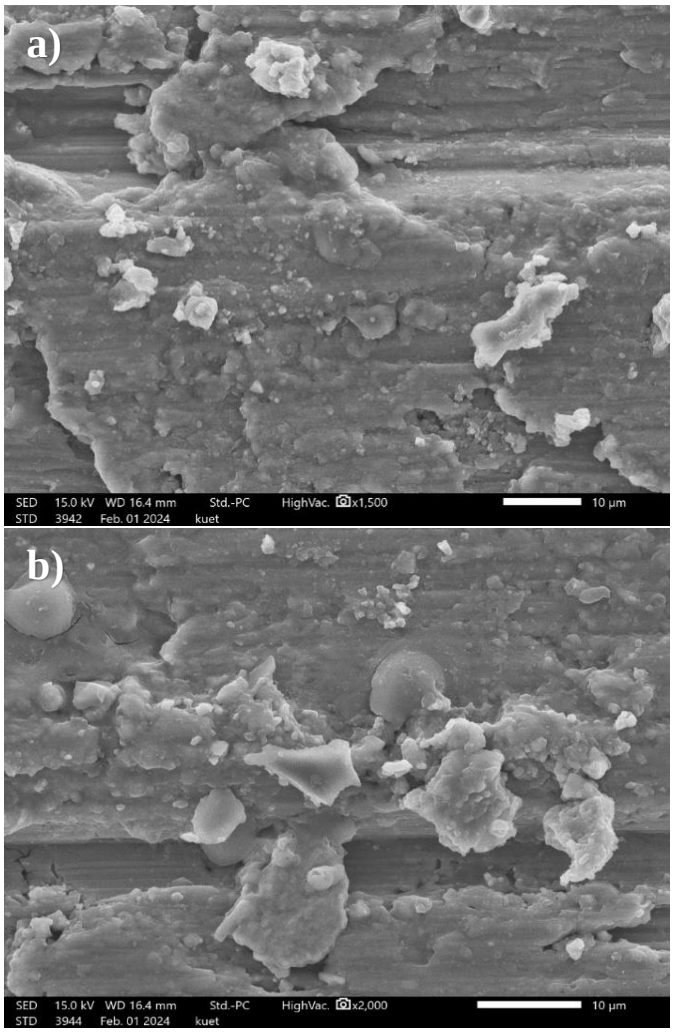

Fig. 6 SEM micrograph of sample (ii) at a) 1500x magnification, b) 2000x magnification.

Significantly, the sample exhibits a notable abundance of granular particles of different sizes, as depicted in Fig. 6. The distribution curve depicted in Fig. 7 represents a normal distribution curve with an average grain diameter of 1.18 microns and a standard deviation of 0.41909. Approximately 30% of the grains in the sample (ii) have diameters ranging from 1 to 1.25 microns, whereas the remaining 70% have sizes that vary.

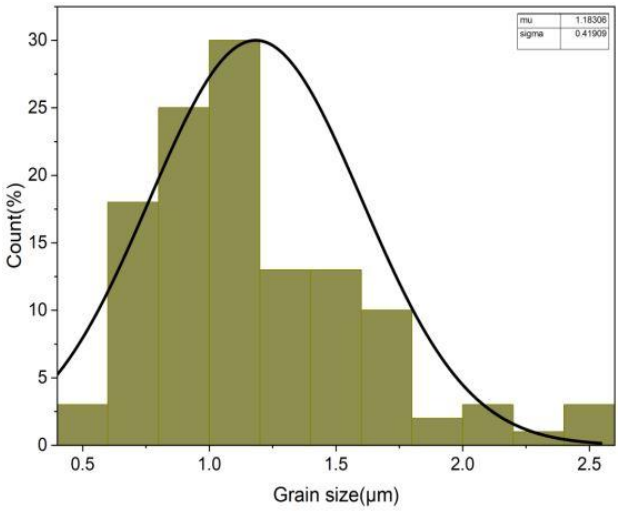

Fig. 7 Normal distribution curve of sample (ii)

The analysis reveals a significant presence of diverse grain sizes, highlighting the homogeneous nature of the sample. These findings underscore the complexity of the material structure and emphasize the importance of accurately characterizing grain size distribution for understanding its properties and potential applications. The use of advanced imaging and analytical tools such as Image J and Origin Pro facilitates precise examination, enabling insights into the microstructural features critical for material performance evaluation and optimization.

3.1.3 Energy Dispersive Spectroscopy

The EDS of the sample (ii) (Al 90% + Al_2O_3 5% + TiO_2 5%) is displayed below in Fig. 8. Al has the highest peak in this sample out of all of them. The elements with the lowest peak in the specimen are C, Sn, Cu, Mg, and Au, all of which are present in extremely small amounts. Among all of them, Sn has the lowest peak. It is discovered that Sn is integrated amongst O, C, Sn, Cu, Mg, and Au and has no weight percentage in the composite. In addition to having the effect of reducing ambient gases during the stirrer, applying vacuum to the molten matrix and reinforcement mixture also tends to dissolve, entrap, and adsorb gases out of the melt during mixing. Sample (ii) has very little oxygen in it after manufacture because the composite is well-insulated from the environment during the process.

We observed peaks for Al and O, confirming the presence of Al_2O_3 in the sample. However, the EDS analysis did not show a Ti peak, which could be due to several reasons, such as the agglomeration of TiO_2 particles, surface preparation issues, or peak overlap. Nonetheless, in the next sections, we will observe a decreasing trend in hardness and an increasing trend in impact strength with the addition of TiO_2 reinforcement in the matrix, attributed to the soft and low-density nature of Ti.

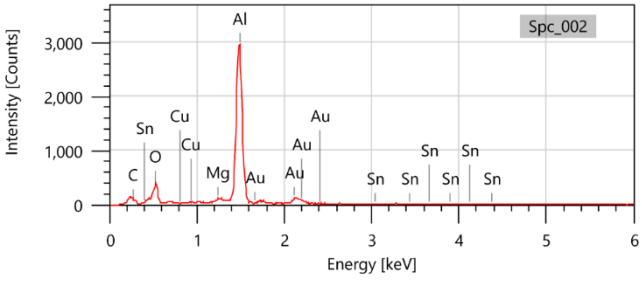

Fig. 8 EDS spectrum of sample (ii).

3.2 Hardness Number

Fig. 9 displays the hardness of various composite specimens. From [31], the hardness of Al 6351 is 109 BHN. Significantly, when the amount of reinforcement increases, the hardness of the composite decreases. Sample (iii) demonstrates the lowest recorded hardness value of 74.84 BHN, mostly attributed to its elevated titanium concentration. In contrast, sample (i) demonstrates the maximum recorded hardness value of 96.33 BHN due to its relatively lower titanium content. Fig. 9 serves to visually represent the comparative Brinell Hardness Numbers of the sample composites, offering insights into the discernible differences in hardness relative to varying titanium concentrations.

The differences in hardness values across the samples highlight the direct influence of titanium concentration on the hardness of the composite. The greater concentration of reinforcement, which is probably the result of reinforcement particle agglomeration and a decrease in matrix wettability, is responsible for the composite's decreased hardness. The agglomeration of reinforcement particles reduces their exposed surface area, affecting the wettability of the aluminum matrix. These particle clusters disrupt uniform dispersion, resulting in poor bonding and decreased wettability in certain regions. Furthermore, when the reinforcing content increases, the density of the composite drops. During mechanical testing, the presence of titanium particles produces voids that provide ideal conditions for the nucleation and development of cracks. The soft and low-density nature of titanium is the main cause of the decrease in the overall hardness of the composite material. The reduced hardness seen in composites reinforced with titanium oxide can be explained by this phenomenon. The results showed a similar pattern to what Ahamad et al. described [31].

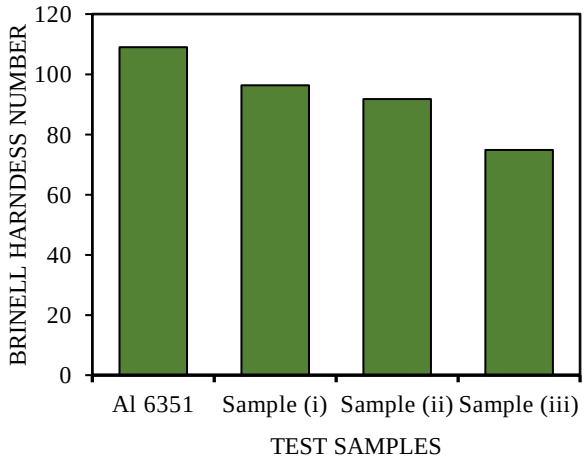

Fig. 9 Brinell Hardness Number of composite samples.

3.3 Tensile Behaviors

Tensile strength, Ultimate Tensile Strength (UTS) and Yield strength are evaluated from the load-displacement curve as well as the stress-strain curve.

3.3.1 Sample (i) Tensile Properties

For sample (i) (95% Al + 2.5% Al2O3 + 2.5% TiO2) from Fig. 10, it is observed that the peak load is 2.7 kN whereas, the displacement at peak load is 0.45 mm. The maximum strength of the specimen is represented by the peak load of the sample (i) which we can see in Fig. 11. At peak load stress-strain curve gives the value of UTS which is 34.38 MPa. Fig. 8 displays that

the initially applied load varies up to the peak point thereafter peak point decreases with increasing applied load. At the breaking point, the load diminishes to 2.6 kN with a displacement of 0.50 mm. The tensile strength at the breaking load is measured at 33.10 MPa, as depicted by the stress-strain curve. Additionally, the yield strength is determined from the stress-strain curve, yielding a value of 22 MPa. Fig. 10 for the load-displacement curve and Fig. 11 for the stress-strain curve is illustrated below.

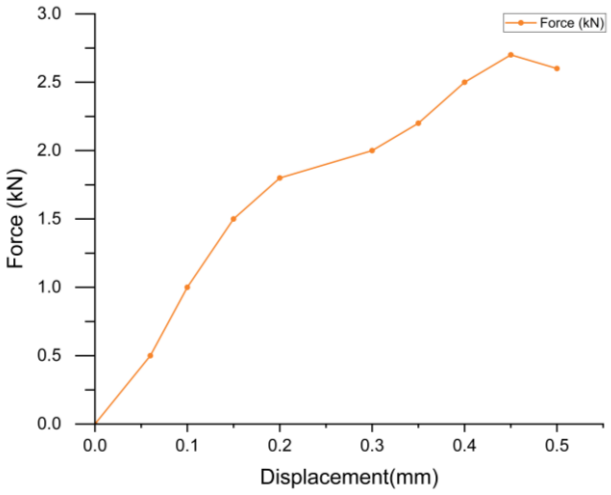

Fig. 10 Load Vs displacement curve for sample (i).

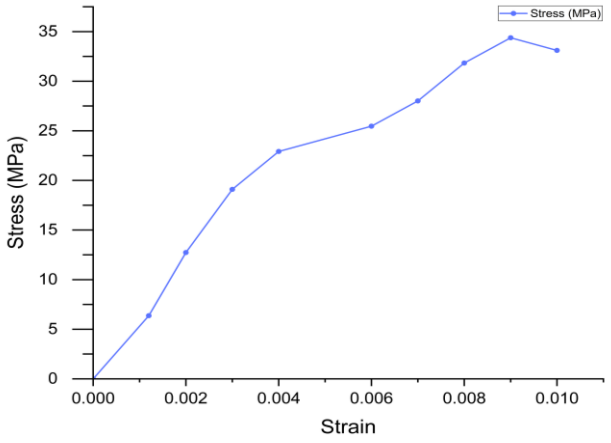

Fig. 11 Stress Vs Strain curve for sample (i).

3.3.2 Sample (ii) Tensile Properties

In Fig. 12, sample (ii) consisting of 90% Al, 5% Al2O3, and 5% TiO2, has a displacement of 0.60 mm at peak load and a peak load of 5 kN. Fig. 13 displays the stress-strain relationship for sample (ii), illustrating the tensile properties of the specimen. The stress-strain curve reaches its maximum load at a value of 63.66 MPa, which is known as the UTS. At the breaking point, the force reduces to 4.8 kN while causing a displacement of 0.65 mm. The stress-strain curve indicates that the tensile strength at the point of fracture is 61.12 MPa, whereas the yield strength is also 40 MPa.

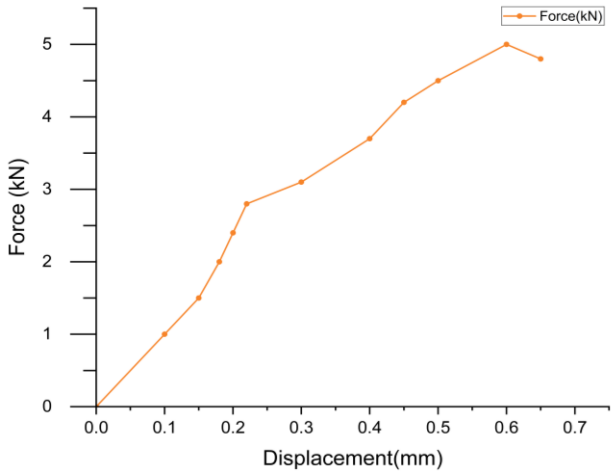

Fig. 12 Load Vs displacement curve for sample (ii).

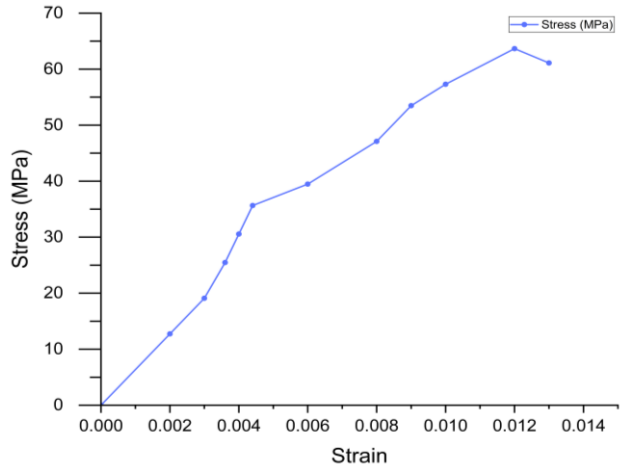

Fig. 13 Stress vs Strain curve for sample (ii).

3.3.3 Sample (iii) Tensile Properties

The peak load for sample (iii) (85% Al + 5% Al2O3 + 2.5% TiO2) in Fig. 14 is observed to be 3.5 kN, whereas the displacement at peak load is 0.50 mm. Fig. 15 shows the stress-strain curve for sample (iii). The stress-strain curve at peak load yields the UTS value of 44.56 MPa. The load decreases to 3.4 kN with a 0.55 mm displacement at the breaking point. The stress-strain curve shows that the tensile strength at the breaking load is 33.10 MPa and yield strength 24 MPa.

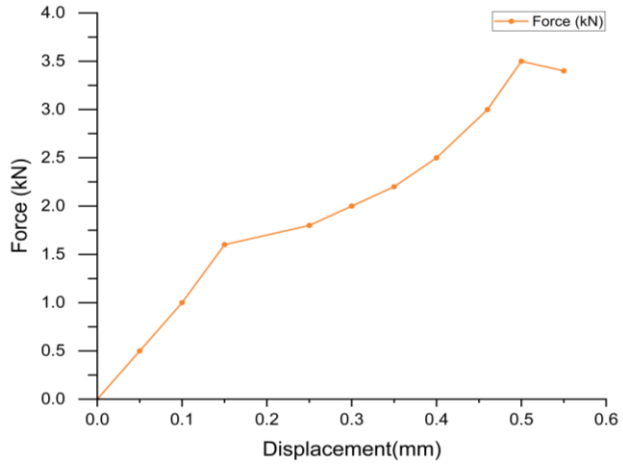

Fig. 14 Load Vs displacement curve for sample (iii).

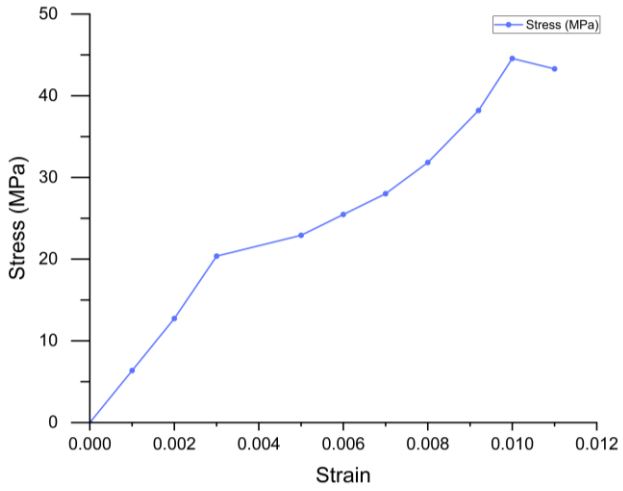

Fig. 15 Stress Vs Strain curve for sample (iii).

3.3.4 Comparative Analysis of Tensile Behaviors

Based on the analysis, it has been determined that the tensile properties of the three samples exhibit variances due to differences in reinforcement. The tensile strength, UTS, and yield strength for sample (i) are 33.10 MPa, 34.38 MPa, and 22 MPa, respectively. In sample (ii), the tensile characteristics showed a substantial increase. The tensile strength, UTS, and yield strength were measured at 61.12 MPa, 63.66 MPa, and 40 MPa, respectively. It has been observed that the tensile characteristics of the composite increase as the reinforcing percentage increased. However, in the case of sample (iii), we observed a tensile strength of 43.29 MPa, an UTS of 44.56 MPa, and a yield strength of 24 MPa. These values are lower than those of sample (ii) but higher than those of sample (i). Based on the SEM images of the sample (ii), we observed a consistent dispersion of reinforcing material throughout the matrix. This uniform distribution contributes to the sample's superior tensile capabilities compared to the other two samples. Below Table 2 shows the maximum tensile load data of the composite samples.

Table 2 Maximum tensile load data of the composite samples.

Sample no.	Diameter, D(mm)	Initial Length, L(mm)	Maximum tensile load, F(kN)
i	10	50	2.7
ii	10	50	5
iii	10	50	3.5

From the observations, it is found that on an increasing percentage of reinforcement in the Al matrix up to 10%, tensile properties increase significantly. Because up to 10% reinforcement, there is a uniform distribution of reinforcement throughout the Al matrix. But when the weight percentage of reinforcement in the Al matrix is above 10%, tensile properties decrease.

A well-dispersed composite allows for improved load transmission because of the more consistent bonding between the matrix and the reinforcing particles (Al_2O_3 and TiO_2). Nevertheless, weak interactions between the matrix and the dispersed particles may result from a heterogeneous distribution. When tensile stress is applied, poor bonding at these interfaces makes it simpler for the material to crack, which lowers the material's overall strength. Also, Particle clustering results in cavities or additional defects in the material. The material is weakened by these voids because they decrease the effective cross-sectional area that bears the tensile force. Because of internal stress concentrations, clusters themselves may serve as sites where cracks begin. The equal distribution of reinforcement, on the other hand, facilitates effective load transmission from the matrix material to the reinforcement, increasing the composite's tensile strength. So, because of the non-uniformity and the influence of reinforcing particle segregation in tensile test specimen, it has been shown that an increase in Al_2O_3 and TiO_2 particles above 10% lowers tensile strength. Fig. 16 illustrates the comparative tensile behavior of the samples.

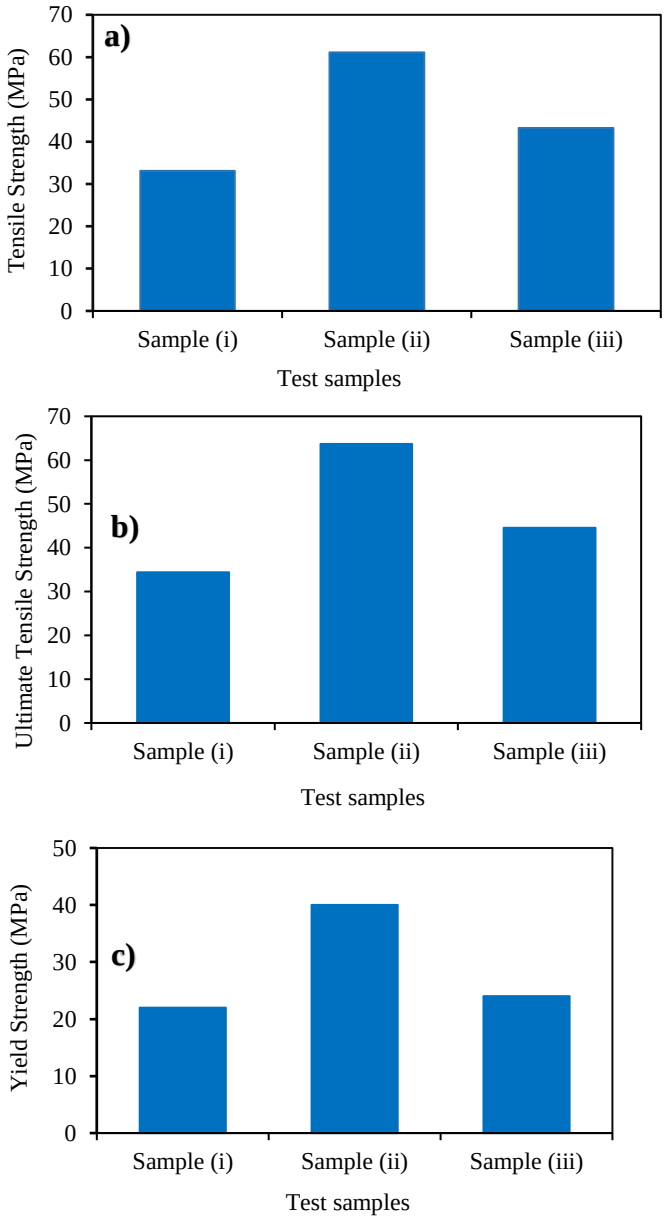

Fig. 16 a) Tensile strength, b) UTS, and c) Yield strength of composite samples.

3.4 Impact strength

The Charpy impact test was done where the V-notch specimens of the composites were used. The test was done by a digital impact tester with a simple pendulum hammer. Ahamad

et al. found that the impact strength of Al 6351 is 29 J [31]. Fig. 17 illustrates the impact strength of the samples. The impact strength of sample (i) is measured to be 32.7 J, while the impact strength of sample (ii) is somewhat higher at 41.8 J. However, in the sample (iii), we observed a substantial and notable increase in impact strength, measuring 54.5 J. It is observed that the hybrid composite specimen's impact strength is contingent upon the percentage of reinforcement present.

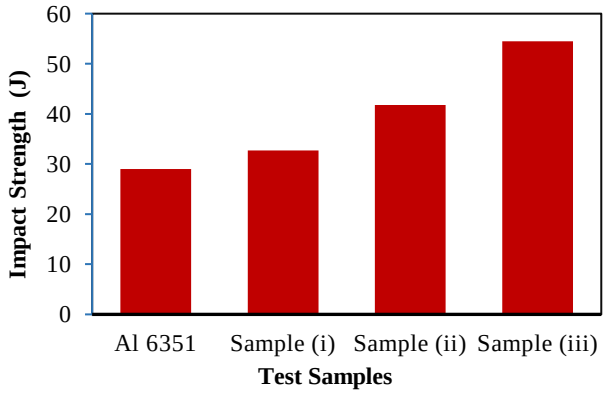

Fig. 17 Impact Strength of composite samples.

Research has shown that the addition of reinforcement to the aluminum matrix leads to an increase in the impact strength of the composite. As the amount of reinforcement rises, the surface of the composite becomes softer, and its ability to withstand impact increases, allowing it to tolerate higher forces before breaking. Therefore, sample (iii) containing 15% reinforcement has the highest impact energy. The findings displayed a pattern that was comparable to that reported by Ahamad et al. [31].

4 Conclusion

The fabrication of stir-casted hybrid AMMCs augmented with Al_2O_3 and TiO_2 was the main emphasis of this research. Stir casting has been used to combine the fine aluminum powder with different combinations of Al_2O_3 and TiO_2(2.5% Al_2O_3+2.5% TiO_2, 5%Al_2O_3+5% TiO_2, 7.5% Al_2O_3+7.5% TiO_2). And also explored mechanical characteristics such as tensile strength, hardness, impact strength and microstructure analysis using SEM. The concluded remarks of the present experimental study are as follows:

The stir casting technique was successfully employed to make these composites, resulting in enhanced mechanical properties such as increased tensile strength and impact strength. The impact of varying the concentration of reinforcement on these parameters has been investigated by altering the content of Al_2O_3 and TiO_2.

The SEM micrographs reveal a consistent dispersion of reinforcement throughout the aluminum matrix, as well as the grain size distribution of the composite. Approximately 30% of the grains have a size between 1-1.25 microns. The average diameter of the grain is 1.18 microns. It has shown the uniform distribution of the reinforcement in the Al matrix.

The Brinell Hardness Numbers for sample (i), sample (ii), and sample (iii) are 96.33 BHN, 91.79 BHN, and 74.84 BHN respectively. The hardness test showed that sample (iii), which had a higher reinforcement of 7.5% Al_2O_3+7.5% TiO_2, had a lower hardness compared to the other specimens. The incorporation of TiO_2 powder into the Al matrix results in a reduction in the hardness of the composite material, which is advantageous for applications requiring lightweight materials.

Sample (i), (ii), and (iii) had tensile strengths of 33.10 MPa, 61.12 MPa, and 43.29 MPa, in that order. Sample (ii) reinforced with 5% Al_2O_3 and 5% TiO_2 have the maximum value of tensile strength. Al matrix gives decreasing tensile strength when the weight percentage of reinforcements in the Al matrix is greater than 10%.

Impact strength increases with an increase in reinforcement content in the composite and the maximum impact strength is 54.5 J for the sample with reinforcement of 7.5% Al_2O_3+7.5% TiO_2. While for sample (i) and sample (ii) impact strengths are 32.7 J and 41.8 J respectively.

This study can be further improved by taking some precautions and steps. So, the following recommendation can be mentioned after conducting the experimental investigation for future researchers:

AMMC with the same composition and experimental procedure might exhibit brittle behavior in one experiment and ductile behavior in another because of temperature, microstructure variations, testing conditions and material aging. So have to be cautious during the whole fabrication process.

In order to improve mechanical properties and give better uniformity among different particles, this study can be expanded by utilizing modern manufacturing techniques such as infiltration, plasma sintering, hot pressing and powder metallurgy.

References

[1] Ramanathan, A., Krishnan, P.K. and Muraliraja, R., 2019. A review on the production of metal matrix composites through stir casting–Furnace design, properties, challenges, and research opportunities. Journal of Manufacturing processes, 42, pp.213-245.

[2] Sharma, A.K., Bhandari, R., Aherwar, A. and Rimašauskienė, R., 2020. Matrix materials used in composites: A comprehensive study. Materials Today: Proceedings, 21, pp.1559-1562.

[3] Ramnath, B.V., Elanchezhian, C., Annamalai, R.M., Aravind, S., Atreya, T.S.A., Vignesh, V. and Subramanian, C., 2014. Aluminium metal matrix composites–a review. Rev. Adv. Mater. Sci, 38(5), pp.55-60.

[4] McDanels, D.L., 1985. Analysis of stress-strain, fracture, and ductility behavior of aluminum matrix composites containing discontinuous silicon carbide reinforcement. Metallurgical transactions A, 16, pp.1105-1115.

[5] Balaraj, V., Kori, N., Nagaral, M. and Auradi, V., 2021. Microstructural evolution and mechanical characterization of micro Al2O3 particles reinforced Al6061 alloy metal composites. Materials Today: Proceedings, 47, pp.5959-5965.

[6] Sajjadi, S.A., Ezatpour, H.R. and Beygi, H., 2011. Microstructure and mechanical properties of Al–Al2O3 micro and nano composites fabricated by stir casting. Materials Science and Engineering: A, 528(29-30), pp.8765-8771.

[7] Krishna, M.V. and Xavior, A.M., 2014. An investigation on the mechanical properties of hybrid metal matrix composites. Procedia Engineering, 97, pp.918-924.

[8] Saravanan, S.D. and Kumar, M.S., 2013. Effect of mechanical properties on rice husk ash reinforced

aluminum alloy (AlSi10Mg) matrix composites. Procedia Engineering, 64, pp.1505-1513.

[9] Ahmadifard, S., Kazemi, S. and Heidarpour, A., 2018. Production and characterization of A5083–Al2O3–TiO2 hybrid surface nanocomposite by friction stir processing. Proceedings of the Institution of Mechanical Engineers, Part L: Journal of Materials: Design and Applications, 232(4), pp.287-293.

[10] Yu, P., Mei, Z. and Tjong, S.C., 2005. Structure, thermal and mechanical properties of in situ Al-based metal matrix composite reinforced with Al2O3 and TiC submicron particles. Materials Chemistry and Physics, 93(1), pp.109-116.

[11] Ahamad, N., Mohammad, A., Sadasivuni, K.K. and Gupta, P., 2020. Phase, microstructure and tensile strength of Al–Al2O3–C hybrid metal matrix composites. Proceedings of the Institution of Mechanical Engineers, Part C: Journal of Mechanical Engineering Science, 234(13), pp.2681-2693.

[12] Bandil, K., Vashisth, H., Kumar, S., Verma, L., Jamwal, A., Kumar, D., Singh, N., Sadasivuni, K.K. and Gupta, P., 2019. Microstructural, mechanical and corrosion behaviour of Al–Si alloy reinforced with SiC metal matrix composite. Journal of Composite Materials, 53(28-30), pp.4215-4223.

[13] Lokesh, N., Manoj, B., Srikanth, K., Ramanayya, P.K.V. and Rao, M.V., 2018. Mechanical characterization of stir cast Al 6063 TiO2-Cu reinforced hybrid metal matrix composites. Materials Today: Proceedings, 5(9), pp.18383-18392.

[14] Abbass, M.K. and Fouad, M.J., 2015. Wear characterization of aluminum matrix hybrid composites reinforced with nanoparticles of Al2O3 and TiO2. Journal of Materials Science and Engineering B, 5(9-10), pp.361-371.

[15] Ahamad, N., Mohammad, A., Sadasivuni, K.K. and Gupta, P., 2021. Wear, optimization and surface analysis of Al-Al2O3-TiO2 hybrid metal matrix composites. Proceedings of the institution of mechanical engineers, Part J: Journal of Engineering Tribology, 235(1), pp.93-102.

[16] El Mahallawi, I., Shash, Y., Rashad, R.M., Abdelaziz, M.H., Mayer, J. and Schwedt, A., 2014. Hardness and wear behaviour of semi-solid cast A390 alloy reinforced with Al 2 O 3 and TiO 2 nanoparticles. Arabian Journal for Science and Engineering, 39, pp.5171-5184.

[17] Hamid, A.A., Ghosh, P.K., Jain, S. and Ray, S., 2008. The influence of porosity and particles content on dry sliding wear of cast in situ Al (Ti)–Al2O3 (TiO2) composite. Wear, 265(1-2), pp.14-26.

[18] Zhang, Q., Xiao, B.L., Wang, Q.Z. and Ma, Z.Y., 2011. In situ Al3Ti and Al2O3 nanoparticles reinforced Al composites produced by friction stir processing in an Al-TiO2 system. Materials Letters, 65(13), pp.2070-2072.

[19] Shuvho, M.B.A., Chowdhury, M.A., Kchaou, M., Roy, B.K., Rahman, A. and Islam, M.A., 2020. Surface characterization and mechanical behavior of aluminum based metal matrix composite reinforced with nano Al2O3, SiC, TiO2 particles. Chemical Data Collections, 28, p.100442.

[20] El-Mahallawi, I.S., Shash, A.Y. and Amer, A.E., 2015. Nanoreinforced cast Al-Si alloys with Al2O3, TiO2 and ZrO2 nanoparticles. Metals, 5(2), pp.802-821.

[21] Li, C., Feng, X., Shen, Y. and Chen, W., 2016. Preparation of Al2O3/TiO2 particle-reinforced copper through plasma spraying and friction stir processing. Materials & Design, 90, pp.922-930.

[22] Long, H.E., Tan, Y.F., Hua, T.A.N., Zhou, C.H. and Li, G.A.O., 2013. Tribological properties of nanostructured Al2O3-40% TiO2 multiphase ceramic particles reinforced Ni-based alloy composite coatings. Transactions of Nonferrous Metals Society of China, 23(9), pp.2618-2627.

[23] Nayak, R.K., Mahato, K.K., Routara, B.C. and Ray, B.C., 2016. Evaluation of mechanical properties of Al2O3 and TiO2 nano filled enhanced glass fiber reinforced polymer composites. Journal of Applied Polymer Science, 133(47).

[24] Jamwal, A., Prakash, P., Kumar, D., Singh, N., Sadasivuni, K.K., Harshit, K., Gupta, S. and Gupta, P., 2019. Microstructure, wear and corrosion characteristics of Cu matrix reinforced SiC–graphite hybrid composites. Journal of Composite Materials, 53(18), pp.2545-2553.

[25] Paulraj, D., Jeyakumar, P.D., Rajamurugan, G. and Krishnasamy, P., 2021. Influence of nano TiO2/micro (SiC/B4C) reinforcement on the mechanical, wear and corrosion behaviour of A356 metal matrix composite. Archives of Metallurgy and Materials, 66(3), pp.871-880.

[26] Kanthavel, K., Sumesh, K.R. and Saravanakumar, P., 2016. Study of tribological properties on Al/Al2O3/MoS2 hybrid composite processed by powder metallurgy. Alexandria Engineering Journal, 55(1), pp.13-17.

[27] Luo, T., Wei, X., Zhao, H., Cai, G. and Zheng, X., 2014. Tribology properties of Al2O3/TiO2 nanocomposites as lubricant additives. Ceramics International, 40(7), pp.10103-10109.

[28] Yılmaz, R., Kurt, A.O., Demir, A. and Tatlı, Z., 2007. Effects of TiO2 on the mechanical properties of the Al2O3–TiO2 plasma sprayed coating. Journal of the European Ceramic Society, 27(2-3), pp.1319-1323.

[29] Oddone, V., Boerner, B. and Reich, S., 2017. Composites of aluminum alloy and magnesium alloy with graphite showing low thermal expansion and high specific thermal conductivity. Science and Technology of advanced MaTerialS, 18(1), pp.180-186.

[30] Nayim, S.T.I., Hasan, M.Z., Seth, P.P., Gupta, P., Thakur, S., Kumar, D. and Jamwal, A., 2020. Effect of CNT and TiC hybrid reinforcement on the micro-mechano-tribo behaviour of aluminium matrix composites. Materials Today: Proceedings, 21, pp.1421-1424.

[31] Ahamad, N., Mohammad, A., Sadasivuni, K.K. and Gupta, P., 2020. Structural and mechanical characterization of stir cast Al–Al2O3–TiO2 hybrid metal matrix composites. Journal of Composite Materials, 54(21), pp.2985-2997.

SciEn
Journal of Engineering Advancements Vol. 06(01) 2025, pp 11-15 https://doi.org/10.38032/jea.2025.01.002

Analysis of Production Loss to Enhance the Productivity of a Knitting Floor

Dip Das[1,], Salin Asfi[1], Rezwan us Saleheen[2], Md. Mostafizur Rahman[1], Mohammad Bellal Hoque[1], Badhon Baria[1]*

[1]Department of Textile Engineering, World University of Bangladesh, Dhaka, Bangladesh
[2]Department of Mechatronics Engineering, World University of Bangladesh, Dhaka, Bangladesh

Received: November 30, 2024, Revised: March 24, 2025, Accepted: March 25, 2025, Available Online: March 27, 2025

ABSTRACT

This research investigates numerous approaches for improving the productivity of a particular knitting floor. There are numerous reasons to pursue an immediate reduction in inefficiencies on knitting floors. Several perceptions were implemented to unveil the disputes for initiating an optimum solution for the floor during knitting. Therefore, ten selected machines have been employed with an Adiabatic Cooling System for scrutinizing a comprehensive production efficiency analysis. Hence an equilibrium of both temperature and humidity was achieved on the floor, restraining minimal dust by spraying micro droplets of water. Neither of the mechanisms subsidized the production efficiency between 12% and 17%, which was lower than the esteemed level taken at the maximum time. Consequently, the plant began to receive 2% to 5% more production than usual once the mentioned methods were implemented gradually. Thus, it reduced the yarn breakage preserving humidity and temperature in a synchronized state. Meanwhile, a foremost response has been achieved by reducing the flying dust. Furthermore, the environment of the knitting floor, routine machine maintenance, and the strain on the machine operator all have vital contributions.

Keywords: Knitting Floor, Productivity, Efficiency, Adiabatic Cooling System, Flying Dust, Humidity, Yarn Breakage.

1 Introduction

Knitting is a widely used method in textile production due to its speed and versatility. However, factors such as machine settings, yarn quality, operator skill, and environmental conditions significantly impact production efficiency. Studies have shown that stitch length, yarn tension, and machine maintenance play a crucial role in minimizing defects and maximizing productivity [1]. Regular maintenance reduces downtime and prevents defects caused by accumulated lint or mechanical wear. Additionally, advanced monitoring systems allow real-time tracking of machine performance, contributing to stable production levels [2].

Previous research has highlighted the importance of optimized machine settings and skilled labor in achieving higher efficiency. A study on knitting technology suggested that an effective workflow and well-maintained machinery could reduce yarn breakage and fabric faults, leading to an efficiency increase of up to 15% [3]. Furthermore, implementing technological advancements such as automated quality control mechanisms has been shown to enhance production rates in knitting operations. Environmental conditions in textile manufacturing have a significant impact on yarn quality and knitting performance. Studies indicate that humidity control is essential for reducing yarn breakage, as higher humidity levels improve yarn elasticity and strength, thereby minimizing production losses. A well-balanced temperature and humidity level also prevent excessive fiber fly accumulation, which can lead to defects and machine inefficiencies [4]. Research on environmental control strategies suggests that maintaining optimal humidity levels (55% ± 5% RH) and temperature (25°C ± 1.1°C) can improve machine efficiency and reduce defects in knitted fabrics. Textile production environments equipped with climate control mechanisms, such as humidifiers and ventilation systems, have demonstrated improved production outcomes by mitigating the negative effects of excessive dryness or heat [5].

One of the innovative solutions for maintaining stable environmental conditions in industrial knitting floors is the use of adiabatic cooling systems. These systems operate by evaporating water droplets into the air, absorbing heat, and lowering the surrounding temperature without the need for traditional refrigeration. Adiabatic cooling has been successfully implemented in textile mills to maintain optimal humidity levels, reduce yarn breakage, and improve air quality by minimizing fiber dust in the workspace [6]. Studies on cooling system applications in textile production reveal that adiabatic cooling can enhance production efficiency by 3-6% due to improved working conditions for both machines and operators [7]. Furthermore, the introduction of these systems has been shown to reduce maintenance requirements and extend machine lifespan by preventing overheating and excessive mechanical stress. Overall, the integration of cooling systems, combined with effective environmental controls and optimized machine operations, has the potential to significantly enhance knitting production efficiency [8].

This study addresses a critical gap by examining the impact of adiabatic cooling on knitting floor efficiency, an aspect largely overlooked in previous research. While prior studies focus on isolated factors like machine settings or maintenance, this research takes a holistic approach by integrating environmental control, dust reduction, machine servicing, and yarn handling. Unlike theoretical analyses, it is based on real-world data, and this makes the findings highly relevant for industrial applications. The study specifically aims to identify efficiency gaps in knitting production, assess regular knitting floor operations, and develop practical strategies to enhance productivity. Furthermore, the present work also provides a

*Corresponding Author Email Address: saleheen1@mte.wub.edu.bd Published by: SciEn Publishing Group

comprehensive and cost-effective solution for optimizing knitting production by tackling both environmental and mechanical challenges.

2. Materials and Methods

2.1. Materials

Yarn used for Single jersey-
Composition: [100% Cotton] 100%
Count: 30'S
Color: White, Indigo, Honey dew
Yarn used for Double jersey (Rib)-
Composition: [95% Cotton 5% Elastin] 100%
Count: 28+40D, 32+40D
Color: White, Green, Black

2.2. Machines and Methods:

There are two types of machines are used in this analysis i.e., Circular knitting machine and Hygrometer

$$\text{Target production in knitting} = \frac{\pi DG \times S.L \times \text{No. of Feeder} \times RPM \times Time \times Efficiency}{10 \times 2.54 \times 36 \times 840 \times Count \times 2.2046} \quad (1)$$

where, D= Cylinder Dia (inch), G= Cylinder Gauge, S.L= Stich Length

$$\text{Efficiency (\%)} = \frac{\text{Production Quantity}}{\text{Production}} \times 100\% \quad (2)$$

$$\text{Relative Humidity (\%)} = \text{Dry bulb temperature} - \text{Wet bulb temperature} \quad (3)$$

Here, the Relative Humidity Sling Psychrometry Table was used as a reference.

$$\text{The target Production/kg in 100\% efficiency (8 hours)} = \frac{\pi DG \times S.L \times \text{No. of Feeder} \times RPM \times Time \times Efficiency}{10 \times 2.54 \times 36 \times 840 \times Count \times 2.2046} \quad (4)$$

To collect and calculate the data, five successive actions have been conducted. Actual production was collected as data for two weeks before the suitable measures were taken. Upon the finalization of the essential procedures, actual manufacture was collected as data for two weeks.

The production of these smart textiles involves several disciplines outside of the typical textile domain, each with its vocabulary, specialized concepts, and methodologies [9]. After compiling the production data for two weeks, the following actions were carried out to enhance productivity. Second phase data have been recorded after ensuring such steps -

i. Ensuring standard humidity on the floor

Based on the data collected, it was discovered that when the temperature rises, outside relative humidity reduces significantly, ensuring favorable conditions for the use of adiabatic cooling [10]. Humidity level has a great impact on yarn strength and elasticity. The increased humidity strengthens the yarn, reducing breakage while maintaining great efficiency. So, to do this, an Adiabatic cooling system is adopted in which water is used to cool the air without the need for traditional refrigeration mechanisms. The cooling system combines the benefits of both dry and adiabatic cooling into a single [11]. The cooling system combines the benefits of both dry and adiabatic cooling into a single unit. Water is sprayed or dripped into the air stream or onto surfaces where it evaporates rapidly. This evaporation process absorbs heat from the surrounding air, lowering its temperature. Recommended conditions for prevention of the breakage are Temperature= 25°C ± 1.1°C and RH%=55% ± 5% RH. Increased humidity makes the yarn stronger, resulting in fewer breakages and more efficiency [12]-[13].

ii. Reductions of flying dust

Dust is defined as dust present in the air during the knitting or processing of yarn, which can contain a mixture of several components including ground-up plant matter, fiber, bacteria, fungi, soil, and pesticides [14]. This fiber fly causes substantial indoor pollution [15]. Data on knitting waste was collected to assess the effect of various yarn properties on knitting fly formation [16]. Sometimes flying dust and tufts get stuck in the machine. Dust accumulation in knitting machinery can increase wear and tear, leading to more frequent breakdowns and maintenance needs. This can result in downtime and decreased productivity as machines require cleaning and repairs. By implementing the Adiabatic system on the floor, the water vapor introduced into the air by the adiabatic system can bind with dust particles, causing them to become heavier and settle out of the air more quickly. This can help to reduce the amount of dust circulating in the environment of the knitting floor which will reduce machine breakage.

iii. Balancing machine tension

In practice, knitting tension is significantly influenced by the pattern type and stitch length [17]. As we know during knitting production, yarn is pushed over the previously placed yarn which increases the abrasion among them and leads to yarn breakage. And yarn breakage reduces the production efficiency. So correct tension for knitting operation is maintained to reduce yarn breakage.

iv. Servicing of the knitting machine

Investing in machine servicing not only increases knitting production but also improves operational reliability, quality, and safety. Knitting tension is significantly influenced by the pattern type and stitch length [17]. So, during our research, we ensured that after each program changed, the machine was checked and cleaned properly. Also, no dust or oil leakage is happening.

v. Prevention of yarn entanglement

The amount of yarn breaks is proportional to the quantity of single and plied yarns used. Twist multipliers have an inverse effect on the number of yarn breaks [18]. When the machine pulls the yarn for knitting, the yarn gets tangled when released from the cone. Constantly dealing with yarn entanglement slows down production processes, reduces overall efficiency, irregularities or defects in the knitted fabric, and can jam knitting machines, leading to downtime as operators work to resolve the issue. To prevent this, scotch tape is used at the head of the cone to prevent yarn entanglement.

vi. Prevention of fabric faults

One of the most significant issues in knit fabric production is reducing fabric flaws [19]. By preventing faults such as yarn breaks, drop stitch holes, snagging, vertical stripes, color fly, dirty cloth, oil stains, soil stripes, spirality, broken ends or holes bunching up, needle break, star marks, etc. Can minimize downtime associated with stopping the machines to fix issues.

3. Result and Discussion

3.1 Estimation of Production Efficiency for Jersey Machine

The investigation regarding knitting production had been performed at Liberty knitwear Ltd. (Unit-2), Gazipur, Bangladesh. Initially, the data respecting to the knitting

production of jersey machine were registered prior to the implementation of proposed methods from S/J fabric production. The jersey machine's production data is shown in Table 1 before any measures are taken. On the contrary, following the implementation of the essential steps, the knitting machine data is displayed in Table 2.

Table 1 Production Data of Single Jersey Fabric (Conventional method)

Parameters	M/c 24	M/c 26	M/c 27	M/c 29	M/c 33
Target Per Week, Kg	930	905	1032	930	1067
Week -1, Kg	805	765	875	785	918
Week -2, Kg	808	748	887	798	892
Average Production, Kg	806	756	808	791	905
Efficiency (%)	86.7%	83.6%	85.9%	85.1%	84.8%
Remarks	S/J	S/J	S/J	S/J	S/J

Table 2 Production Data of Single Jersey Fabric (Proposed method)

Parameters	M/c 24	M/c 26	M/c 27	M/c 29	M/c 33
Target Per Week, Kg	930	905	1032	930	1067
Week-1, Kg	825	778	896	805	931
Week-2, Kg	818	796	906	818	923
Average Production, Kg	822	787	901	812	927
Efficiency (%)	88.3%	86.9%	87.3%	87.2%	86.8%
Remarks	S/J	S/J	S/J	S/J	S/J

After reviewing the two data sets from Tables 1 and 2, Fig. 1 can be illustrated. The graph displays a greater level of production efficiency than the existing situation when the necessary actions have been put into place. Before putting those necessary steps into place, production efficiency is found to be between 14 and 17 percent lower.

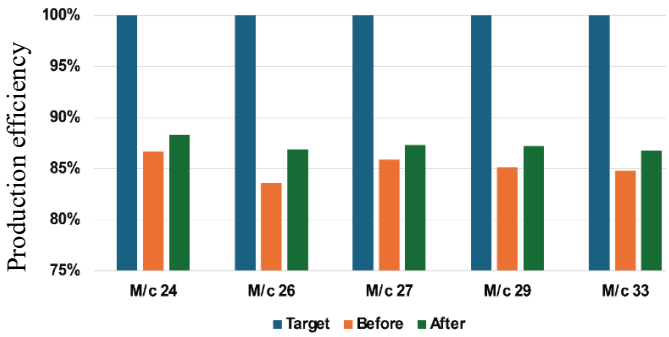

Fig. 1 Efficiency analysis of Single Jersey fabric

However, following implementation, the production efficiency grew by a respectable proportion, ranging from 3 to 6%. For example, after one week at that specific knitting floor, the production of one jersey fabric climbed to an average of 16 kg, 31 kg, 93 kg, 21 kg, and 22 kg for machines 24, 26, 27, 29, and 33. Consequently, it can be said that the manufacturing of Single Jersey fabric has risen with greater production efficiency once all the required steps have been performed.

3.2. Estimation of Production Efficiency for Double Jersey Machine (Rib)

Before executing any of the aforementioned procedures wherein rib fabric was made, the production data of the Double Jersey machine is displayed in Table 3. However, once the required actions have been taken, the knitting machine data is displayed in Table 4.

Table 3 Production Data of Rib Fabric (Conventional method)

Parameters	M/c 07	M/c 09	M/c 11	M/c 64	M/c 74
Target Per Day, Kg	318	425	470	312	312
Week -1, Kg	254	367	388	254	258
Week -2, Kg	275	355	405	278	264
Average Production, Kg	264	361	396	266	261
Efficiency (%)	83.2%	84.9%	84.5%	85.3%	83.7%
Remarks	Rib	Rib	Rib	Rib	Rib

Table 4 Production Data of Rib Fabric (Proposed method)

Parameters	M/c 07	M/c 09	M/c 11	M/c 64	M/c 74
Target Per Day, Kg	318	425	470	312	312
Week -1, Kg	268	365	398	264	278
Week -2, Kg	279	382	415	288	254
Average Production, Kg	273	373	406	276	266
Efficiency (%)	86.1%	87.8%	86.5%	88.5%	85.3%
Remarks	Rib	Rib	Rib	Rib	Rib

Upon reviewing the data from Tables 3 and 4, Fig. 2 can be presented. The graph displays a greater level of production efficiency than the existing situation when the necessary actions have been put into place. Production efficiency was determined to be between 12 and 17 percent lower before the implementation of the aforementioned processes.

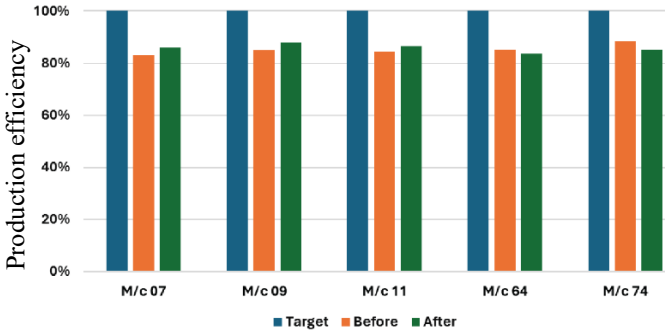

Fig. 2 Efficiency analysis of Rib fabric

However, following implementation, the manufacturing efficiency grew by a respectable amount, between 2 and 5 percent. The production of Double Jersey Rib fabric increased by an average of 9 kg, 12 kg, 10 kg, 10 kg, and 5 kg for machines 07, 09, 11, 64, and 74 after one week at that specific knitting floor. Consequently, it is possible to conclude that, following the necessary steps, rib fabric production has increased with improved production efficiency.

3.3. Estimation of Relative Humidity and Temperature for the knitting floor

Table 5 shows the data of weekly Relative Humidity RH% and Temperature of the knitting floor before implementing any of the above-mentioned. On the other hand, Table 6 shows the data of weekly Relative Humidity RH% and Temperature of the knitting floor after implementing the mentioned steps.

Table 5 RH% and Temperature of knitting Floor (Conventional Method)

Parameters	RH%	Temp. °C	Wet bulb – dry bulb temp.	Yarn breakage (8*6=48) hours
Target/Week,	70% ± 5%	25°C ± 1.1°C	(3-5)°C	72- 120 times
Week-1	59%	28°C	6°C	175 times
Week-2	55%	30°C	7°C	168 times
Average	57%	29°C	6.5°C	171.5 times

Table 6 RH% and Temperature of Knitting Floor (Proposed Method)

Parameters	RH% (1)	Temp. °C (1)	Wet bulb – Dry bulb temp.	Yarn breakage (8*6=48) hours
Target Per Week,	70% ± 5%	25°C ± 1.1°C	(3-5)°C	72- 120 times
Week-1	69%	24°C	4°C	103
Week-2	75%	22°C	3°C	98
Average	72%	23°C	3.5°C	100.5

Based on the study of Tables 5 and 6, Fig. 3 can be illustrated. Following the required actions, the graph displays a lower temperature and a greater relative humidity than in the current situation. As we can see, there was a noticeable decrease in yarn breakage. After doing the required actions, it can be concluded that the knitting floor's temperature decreased and its relative humidity (RH%) rose.

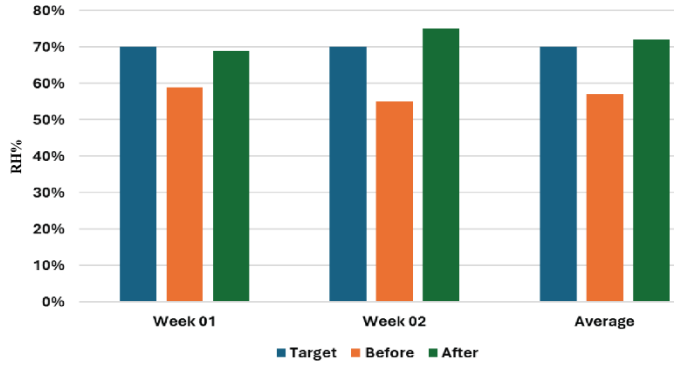

Fig. 3 Relative Humidity (RH%) analysis of the knitting floor

4. Conclusion and Recommendations

The study highlights the significant impact of environmental controls, machine maintenance, and optimized operational procedures on improving knitting floor productivity. The implementation of an adiabatic cooling system effectively stabilized humidity levels, reduced yarn breakage, and minimized airborne fiber dust, leading to a measurable increase in production efficiency. Additionally, ensuring proper machine servicing, tension balancing, and fabric fault prevention contributed to improved operational reliability. To scale up these interventions in larger textile facilities, fully automated climate control systems should be explored to regulate temperature and humidity in real time. This would enhance the consistency of environmental conditions and further reduce production losses due to fluctuating humidity and fiber breakage. The adoption of Internet of Things (IoT)-based solutions for machine performance tracking, humidity regulation, and production efficiency analysis can also provide real-time insights. Smart sensors can alert operators to deviations in environmental conditions, enabling timely interventions. Furthermore, future research should investigate the feasibility of scaling up adiabatic cooling systems for larger knitting operations, including energy consumption analysis and cost-benefit assessments. Hybrid cooling systems combining adiabatic and mechanical cooling could be explored for enhanced efficiency.

Additionally, integrating machine learning algorithms to predict and mitigate potential production disruptions by analyzing historical data on machine performance, environmental factors, and defect rates could optimize the manufacturing process. Further studies should also assess the long-term sustainability of these interventions, particularly in terms of water usage for adiabatic cooling, energy efficiency, and overall environmental impact. Life-cycle assessments of different environmental control strategies can guide the development of more eco-friendly solutions. By implementing these advanced technological solutions, large-scale textile industries can further enhance production efficiency, reduce material waste, and create a more sustainable manufacturing environment.

References

[1] Morshed, N., Ahmed, Z., Alam, A., et al., 2022. Improvement of Dust Resistance Properties on The Surface of Jute Knitted Fabrics, *International Journal of Latest Technology in Engineering, Management & Applied Science (IJLTEMAS), 11*, pp. 11–16.

[2] Roy, R., Laha, A., Roy, S., et al., 2022. Filtration performance of needle-punched nonwoven air filter media through dyeing process. *NIScPR Online Periodicals Repository*, 11, pp.1–10.

[3] Avadanei, M., Vatra, D. and Rosca, M., 2023. The influence of body biomechanics on the geometry of clothing patterns. *Communications in Development and Assembling of Textile Products*, 4, pp.231–241.

[4] Wu, H., Shen, Y., Yao, Y., et al., 2021. Size formulations for cotton yarn weaving at lower relative humidity. *Textile Research Journal*, 91, pp.168–174.

[5] Pavko Čuden, A., 2022. Recent developments in knitting technology. In: *Advanced Knitting Technology*. Elsevier, pp.13–66.

[6] Khan, A.A., Mishra, R. and Jamshaid, H., 2024. Weft knitting machines. In: *Knitting Science, Technology, Process and Materials: A Sustainable Approach*. Cham: Springer Nature Switzerland.

[7] Doe, J., Smith, J. and Johnson, M., 2012. Development of an adiabatic cooling system for efficient heat dissipation in electronic devices. *International Journal of Thermal Sciences*, 91, pp.168–174.

[8] Semnani, D., 2011. Advances in knitting technology. *Journal of Knitting and Textiles*, 191, pp.171–192.

[9] Eichhoff, T., 2013. *Multidisciplinary Know-How for Smart-Textiles Developers*. Woodhead Publishing Limited.

[10] Fairhurst, C. ed., 2008. *Advances in apparel production*. Elsevier.

[11] Mihai, V. and Rusu, L., 2022. Improving the ventilation of machinery spaces with direct adiabatic cooling system. *Inventions*, 7, p.78.

[12] Redelinghuys, L.G., Tshamala, M.C. and Hans, T.M., 2023. Performance of an adiabatic pre-cooling system for concentrating solar power plants in arid areas. *Applied Thermal Engineering*, 231, p.120819.

[13] Baheti, N., Daberao, A.M., Kolte, P.P., et al., 2018. The effect of moisture content on yarn properties and knitability. *Journal of the Textile Association*, 78, pp.309–311.

[14] Zhu, Y., Zhang, J., Zhao, X. and Xu, H., 2024. Analysis of the impact of environmental temperature and humidity on cotton fiber quality during initial processing. *Journal of Natural Fibers*, 21(1), p.2338538.

[15] Kumar, R., 2008. Cotton dust - Impact on human health and environment in the textile industry. *Textile Magazine*, 49, p.55.

[16] Bhowmick, N. and Ghosh, S., 2008. Role of yarn hairiness in knitting process and its impact on knitting room's environment. *WSEAS Transactions on Environment and Development*, 4, pp.360–372.

[17] Pohlen, V., Schnabel, A., Neumann, F., et al., 2012. Optimisation of the warp yarn tension on a warp knitting machine. *AUTEX Research Journal*, 12, pp.29–33.

[18] Almetwally, A.A., Mourad, M. and Mohammed, A.E.E., 2013. A study of yarn breaks on warping machines. *Life Science Journal, 10(1), pp.108-114*.

[19] Ahmed, T., Toki, G.F.I., Mia, R., et al., 2022. Implementation of the Six Sigma methodology for reducing fabric defects on the knitting production floor: A sustainable approach for knitting industry. *Textile and Leather Review*, 5, pp.223–239.

SciEn
Journal of Engineering Advancements Vol. 06(01) 2025, pp 16-21 https://doi.org/10.38032/jea.2025.01.003

Comparative Study of Production of Bio-fuel from Mango Seed Kernel Using Pyrolysis and Chemical Conversion Processes

Md. Mushrafi Al- Mueed[1], Md. Masud Rana[2], Md. Hasan Ali[1,]*

[1]Department of Energy Science and Engineering, Khulna University of Engineering & Technology (KUET), Khulna-9203, Bangladesh
[2]Department of Chemical Engineering, Khulna University of Engineering & Technology (KUET), Khulna-9203, Bangladesh

Received: January 16, 2025, Revised: March 21, 2025, Accepted: March 27, 2025, Available Online: March 29, 2025

ABSTRACT

The conversion of mango seed kernel into biofuel was performed through thermal pyrolysis and chemical transesterification process in this present study. The research also involved a comparative analysis of product yield and physico-chemical properties of the resulting biofuel. The pyrolysis experiment was performed in a 22 cm length and 15 cm diameter fixed bed external heating reactor at a temperature ranging from 150 – 350°C using a full-size sample. The major components of the experimental setup included a furnace, fixed-bed external heating reactor, water-cooled condenser, K-type thermocouples, and collectors for liquid and char. Instead of electricity, low-grade waste biomass was used for heating. This process achieved a maximum biofuel yield of 30.18 wt.%. For the chemical process, initially vegetable oil was extracted through a solvent extraction method, mixing the samples in a 1:2 ratio with hexane and stirring the mixture at a temperature between 25 – 50°C for a duration of 3 – 12 hours, resulting in a 17.3 wt.% yield of vegetable oil. After that, the obtained vegetable oil was transesterified using potassium hydroxide as a catalyst at 60°C for 1 – 1.5 hours. A maximum of 75 – 80 wt.% of extracted vegetable oil was converted into biofuel. The produced biofuels were evaluated for their suitability as alternative fuels by analyzing their physico-chemical properties including viscosity, density, pour point, flash point, and gross calorific value.

Keywords: Bio-fuel; Mango Seed Kernel; Pyrolysis, Transesterification; Product Yields; Fuel Properties.

1 Introduction

The world has been facing increasing energy demand and emphasizing the urgency for sustainable and environmentally friendly solutions. Fossil fuels including natural gas, oil, and coal account for 80 – 85% of total global primary energy production but as these resources are finite, several studies have predicted that they will eventually be depleted over time [1], [2]. However, using these resources is scary because of their high rate of consumption and release of greenhouse gases that contribute to environmental issues [3] including global warming, climate change acid rain, and health issues from the discharge of toxic compounds [4], [5].

In addition, the rise in population, urbanization, and economic development has led to increased waste generation. According to World Bank, if the current rate of waste generation continues it is expected to increase by approximately 70% by 2050 [6] – [8]. From the research studies, carbon dioxide (CO_2) emissions are directly linked to the consumption of fossil fuel and are responsible for worldwide climate changes [9]. To address these challenges, researchers assert that carbon-neutral biomass presents a promising resource for energy production, especially in the form of biofuel [10]. Such substances hold special significance because they are renewable, widely accessible, biodegradable, non-toxic, and environmentally sustainable [11]. They not only help to reduce dependence on fossil fuels but also support the objectives of the Kyoto Protocol which aim to mitigate greenhouse gas emissions [12]. This biofuel is increasingly being acknowledged worldwide as a green fuel because of its low sulfur content, biodegradable properties, and high flash point [13].

The tropical and subtropical climate of the South Asian region is ideal for the prolific growth of fruits like mangoes. Bangladesh is currently in the seventh position globally in terms of mango production [14]. In 2012, global mango production was estimated at approximately 46.7 million MTs and this figure is further increasing [15]. According to authorities from the Department of Agricultural Extension (DAE), the yearly mango production in Bangladesh is expected to reach around 2.55 million MTs in 2023 [16]. In fruit processing industries around 40 – 50% of mangoes are processed into juice and other by-products, while the seeds and peels are typically discarded as waste [17]. Depending on the variety, mango seeds account for 30 – 40% of the fruit's weight [18]. Mango seeds are comprised of two main parts: seed shell and seed kernel. The shell is the outer layer of the seed; it covers the kernel. The shell makes up about 5 – 15% of mango while the kernel accounts for 10 – 20% [19] –[21]. The chemical composition of the mango seed includes lignin, hemicelluloses, and cellulose are primary constituents in the shell while starch and fat are in the kernel [22].

Previously, researchers have produced biofuel from various non-edible biomass sources such as jatropha, microalgae, neem, karanja, rubber seed, mahua, silk cotton tree, castor, pongamia pinnata, and others. These biofuels have shown to be viable alternatives to conventional fuels [23] – [29]. Sultana and Ashraf [29], Saka et al. [30], Julio et al. [31], and Narayansamy et al. [32] have investigated various extraction and chemical processing techniques for biofuel production from mango seeds. They also analyzed different catalyst's impact on product yield and the properties of resulting biofuel. Additionally, Ganeshan et al. [33], Lam et al. [34], Lazzari et al. [35], and Andrade et al.

*Corresponding Author Email Address: hasan@ese.kuet.ac.bd Published by: SciEn Publishing Group

[36] conducted experiments on the pyrolysis of mango seed shell or kernel in a fixed-bed reactor and examined the product yield of biofuel, gas, and char.

Previous experiments entailed milling the samples into the form of powder and utilizing electricity during heating, which was energy-inefficient and incurred additional labor costs. As a result, the main objective of the current research is to produce biodiesel from mango seed kernels through the pyrolysis and transesterification process, including the construction of a pyrolysis reactor that can produce biofuel from mango seed kernels without using electricity. This study also aims to compare the product yields and physico-chemical characteristics of the biofuel obtained from both processes.

2 Materials and Methodology

2.1 Materials

In this study, mango seed kernel was utilized as feed material, which was collected from Khulna City, Bangladesh. Initially, the seeds were properly rinsed with water and detergent to wash away any remnants of mud, sand, or additional surface impurities. Upon washing, the seeds were sun-dried to remove any additional moisture. Once fully dried, each of the seeds was meticulously split using a knife to retrieve the kernel, which originally measured around 4 – 6 cm. Fig. 1 depicts the sample that was prepared for both pyrolysis and transesterification. Although the full-sized kernel was employed in pyrolysis, for transesterification the kernels were pulverized into smaller fragments as this increased the surface area and facilitated the extraction of the oil.

2.2 Experimental Set-Up and Procedure

2.2.1 Pyrolysis Experiment

The pyrolysis of mango seed kernels was carried out using a fixed-bed external heating reactor designed to produce biofuel. The major components of the experimental setup were a fixed-bed external heating chamber, reactor inside the heating chamber, water-cooled condenser for condensing the pyrolytic vapor, K-type thermocouples with display, liquid collecting pot, N_2 gas cylinder with flow control valve and pressure regulator, char collecting bag and fan. Fig. 2 illustrates a diagram of the experimental setup offering a visual representation of the configuration. The setup included a furnace constructed from galvanized steel, which measured 61 cm in length and 36 cm in diameter. Inside this chamber, an aluminum reactor of 22 cm in length and 15 cm in diameter was positioned. The size of the reactor was finalized after analyzing the size taken by different researchers for their experiments [4], [26], [37], [38]. In each pyrolysis run 0.5 kg of pre-treated mango seed kernel was placed into the reactor chamber via the top opening. Before initiating the pyrolysis experiment, the reactor was purged with N_2 gas for 2 – 3 minutes to create an inert atmosphere. The experiments were conducted by changing the temperature between 150 – 350°C with an interval of 50°C, with the inside temperature of the reactor closely monitored using K-type thermocouples. Although higher temperatures and rapid heating using electricity can produce higher biofuel yields, a relatively low temperature (150-350°C) and slow heating were used in this study due to the use of low-grade waste biomass for heating. Additionally, maintaining a high temperature using waste biomass is quite impossible.

(a) (b)

Fig. 1 Prepared feedstocks of mango seed kernel for (a) pyrolysis (b) transesterification

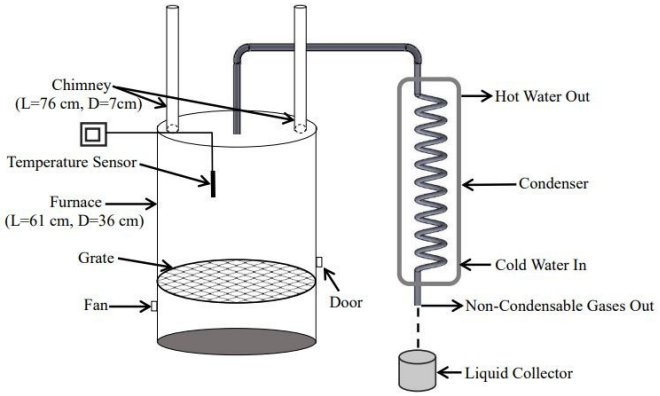

Fig. 2 Schematic diagram of pyrolysis system

Lazzari et al. [35] investigated the rise in liquid yield during the pyrolysis of mango seed kernels at temperatures ranging from 200°C to 450°C and Dyjakon et al. [39] examined the physico-chemical properties of mango, lychee, and avocado seeds at temperatures between 200 – 300°C, observing that higher temperatures led to increased production and higher heating values.

During the combustion of low-grade waste biomass, which served as the heating source, the produced smoke was vented through two chimneys, each measuring 76 cm in length and 7 cm in diameter. The volatile gases coming from the reactor were then cooled by passing through a water-cooled copper condenser, where the condensable gases were converted into liquid and collected in a pot. Non-condensable gases were flared into the open air separately. The heating process continued until all gases were completely released from the biomass indicating the completion of the pyrolysis reaction and the total duration was recorded as the reaction time for the process. Initially, as the temperature increased, the production of liquid also increased until it reached its maximum level, after which it began to decrease. The maximum liquid production occurred at an optimum temperature of 250°C, as the raw material undergoes significant breakdown at this temperature. However, beyond 250°C, liquid production decreased while gas production increased. The decline in liquid production and rise in gas production are likely due to secondary decomposition processes and the transformation of some oil vapors into permanent gases. After the pyrolysis reaction was complete heating was ceased and the set-up was allowed to cool. The reactor was then opened to extract char residue and weigh it after putting it into a sample bag. Similarly, the weight of the obtained liquid was also measured. The weight of pyrolytic gas was determined by subtracting the combined weight of char and liquid from the

initial weight of the feedstock. The system was then prepared for subsequent runs ensuring a systematic and efficient approach to the experimental process.

2.2.2 Transesterification Experiment

The production of biofuel from mango seed kernels involves two main steps: firstly, extracting vegetable oil from the kernels and secondly, converting that vegetable oil into biofuel. Vegetable oil was extracted from mango seed kernel using hexane through a solvent extraction method. Each test involved mixing 100gm of the sample with hexane at ratios of 1:2.5 or 1:2 (w/v), followed by agitation. Agitation was conducted at temperatures ranging from 25 to 50°C for 3 – 12 hours to optimize the chemical reaction throughout the solvent and sample for maximizing oil extraction. Before agitation, the material was submerged in hexane for approximately 48 hours. After that, the vegetable oil was separated using evaporation and filtration techniques. A flow chart illustrating the biofuel production process through transesterification is provided in Fig. 3.

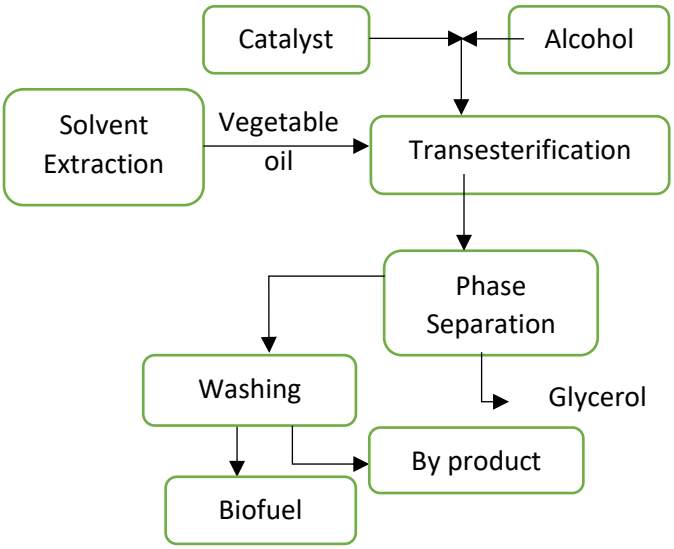

Fig. 3 Transesterification process to produce biofuel

For producing biofuel from the extracted vegetable oil transesterification process was utilized. This reaction was conducted at 60°C for 1 hour where the vegetable oil was forcefully agitated with a methanol-KOH solution. To drive the reaction toward biofuel production, a methanol-to-oil molar ratio of 6:1 was used by adding an excess of methanol. Zhang et al. [40] determined the required amount of KOH in kilogram for the transesterification using the formula, KOH = 0.013 × Volume of vegetable oil (liters). Therefore, KOH was incorporated at a level of 1.5% of the oil's weight. At a constant temperature, the reaction was continued for 1 – 1.5 hours and then it was left for 24 hours to settle. This settling resulted in biofuel floating on top, while glycerin accumulating at the bottom. Both biofuel and glycerin were carefully separated. Filtration was also carried out to remove free fatty acids, enhancing the quality of the biofuel.

2.3 Product Analysis Procedure

Characterization is essential to assess the efficiency and acceptability of the produced biofuel for different purposes. Standard ASTM test procedures were used to examine various types of physico-chemical characteristics, such as viscosity, pour point, density, gross calorific value (GCV), and, flash point. The oil's density indicates how aromatic it is, while its kinematic viscosity shows its flow characteristics. Density and viscosity measurements were performed using the ERASPEC Fuel Analyzer-ES10. The flash point, which is the minimum temperature at which the fuel momentarily ignites without sustaining a flame, was determined using the Pensky-Martens AIM 509 (Closed) apparatus. The pour point, indicating the temperature at which the biofuel ceases to flow, was assessed using the AEX 503 device. Finally, the calorific value, representing the energy or heat released upon combustion, was measured with the GDY-1C Oxygen Bomb Calorimeter.

3 Results and Discussion

3.1 Proximate Analysis

Mango seed kernel's proximate analysis identifies their compositional attributes, including moisture content, volatile matter, ash content, and fixed carbon content. These tests were conducted following ASTM standards. The result of this analysis for mango seed kernel is presented in Table 1.

Table 1 Proximate analysis of mango seed kernel

Parameters	Mango Seed Kernel
Volatile Matter (%)	67.53
Ash Content (%)	3.9
Moisture Content (%)	11.13
Fixed Carbon (%)	17.44

3.2 Product Yields

The biofuel obtained through the pyrolysis and transesterification of mango seed kernel is illustrated in Fig. 4. Pyrolysis experiments were conducted at temperatures ranging from 150°C to 350°C at 50°C increments, resulting in the production of three distinct types of products: liquid, solid, and gas. The maximum yield of pyrolytic liquid and solid were 30.16 wt.% and 65.23 wt.% at a temperature of 250°C and 150°C, respectively. The yields of pyrolytic liquid varied significantly with temperature and were affected by various factors which include the feedstock layout, temperature of operation, reactor size as well as type, heat transfer efficiency from the reactor surface to the biomass, feed size of particles, and vapor time of residence [37].

(a) (b)

Fig. 4 Biofuel derived from mango seed kernel (a) pyrolysis (b) transesterification

In contrast, 13.8% of the vegetable oil was recovered using the solvent extraction method from the mango seed kernel. Subsequently, through the transesterification process 75 – 80% of this vegetable oil was converted into biofuel. It is recommended that using Soxhlet instead of Hexene and reducing the feed size can potentially improve the vegetable oil recovery.

3.3 Properties of Produced Bio-fuel

The biofuel derived from the pyrolysis of mango seed kernel was dark red-brown and had a strong acrid odor. Notably, if the water content exceeds 30 – 40 wt.% phase separation can occur [41]. The pyrolytic liquid was homogeneous and in the liquid storage bottles, there was no phase separation. In contrast, the biofuel produced via transesterification exhibited a yellowish color. Several physico-chemical characteristics of the obtained biofuel through pyrolysis and transesterification including density, kinematic viscosity, flash point, pour point, and calorific value were measured and compared. The results are summarized in Table 2.

The density of the liquid obtained through pyrolysis (875.4 kg/rn^3) exceeds that of diesel but closely resembles biodiesel fuels, such as those derived from jatropha (880 kg/rn^3), neem (878 kg/rn^3), and waste cooking oil (910 kg/rn^3). In contrast, liquid obtained through transesterification (778.8 kg/rn^3) is lower than diesel, jatropha, neem, and waste cooking oil. Generally, fuels with higher density result in lower fuel consumption, while those with lower density require more to produce the same heat output. The kinematic viscosity of biofuel produced through pyrolysis and transesterification is 2.86 and 1.74 cSt, respectively, at 40°C, which is similar to diesel (2 – 4.5 cSt at 40°C) but lower than those of jatropha (4.8 cSt), neem (5.81 cSt), and waste cooking oil (4.9 cSt).

Lower viscosity is beneficial for easier handling and transportation. The viscosity of biofuel can vary widely depending on the feedstock, process conditions, and the efficacy of low-boiling component collection [42]. The flash point of biofuel from pyrolysis and transesterification is 112°C and 70°C, respectively, which are higher than diesel (50 – 95°C). In contrast, jatropha (135°C) [43], neem (175°C) [7], and waste cooking oil (150°C) [44], the flash points of biofuel from pyrolysis (112°C) and transesterification (70°C) exhibit significantly lower. This is because biomass-derived liquids are less refined and contain a variety of components with a wide distillation range. The pour point of biofuel through pyrolysis and transesterification is –11°C and –9°C, respectively. Although these pour points are lower than diesel, the practical experience of the present study suggested that this was not problematic. However, despite these promising properties, the gross calorific value of the biofuel from pyrolysis is 18.8 MJ/kg, and from transesterification is 22 MJ/kg which is considerably lower than that of diesel (42–46 MJ/kg), jatropha (39.5 MJ/kg), neem (26.65 MJ/kg), and waste cooking oil biodiesel (35.5 MJ/kg) due to the presence of moisture and oxygenated chemicals.

Even though, the liquid oils obtained from pyrolysis and chemical conversion have certain challenges that may affect combustion, engine efficiency, and emissions [37], appropriate treatment is necessary to make them suitable for use in engines.

4 Conclusions

This study focused on producing biofuel from the mango seed kernels exploring its viability as an alternative fuel. Pyrolysis was carried out in a fixed-bed external heating reactor at a temperature ranging from 150 – 350°C for full-sized samples. For the chemical process initially, vegetable oil was extracted through a solvent extraction method, mixing the samples with hexane in a 1:2 ratio and the mixture was agitated between 25 – 50°C for a duration of 3 – 12 hours. The obtained vegetable oil was subsequently turned into biofuel via the transesterification process, utilizing potassium hydroxide as the catalyst at 60°C for 1 – 1.5 hours. The results of this experiment likely provide insights into product yields, chemical composition, and potential applications of the biofuel produced.

- The maximum yield of biofuel from full-sized mango seed kernel through pyrolysis was 30.18 wt.% at a temperature of 250°C.
- The chemical conversion process extracted 17.3 wt.% vegetable oil from mango seed kernel, with a maximum of 75 – 80 wt.% of this oil was converted into biofuel.
- Analysis of the physico-chemical properties revealed that both the biofuels were dense with moderate viscosity and had favorable pour and flash point.
- The calorific value of biofuel produced through pyrolysis and transesterification process was 18.08 MJ/kg and 22 MJ/kg, respectively.
- The biofuel derived from mango seed kernel can be utilized either as a low-grade biofuel or as a blend with conventional liquid fuel.

As a waste product from mango processing industries and an alternative energy source, future studies can focus on how companies can implement this process economically. This

Table 2 Comparison of properties of biofuel derived through pyrolysis and transesterification with conventional diesel, and other biofuel sources

Properties	Mango seed kernel oil		Diesel	Jatropha Biodiesel [43]	Neem Biodiesel [7]	Waste Cooking Oil [44]
	Pyrolysis	Trans-esterification				
Density (kg/m^3), 30°C	875.4	778.8	820 to 860	880	878	910
Kinematic Viscosity (cSt)	2.86	1.74	2 to 4.5	4.8	5.81	4.9
Flash Point (°C)	112	70	50 to 95	135	175	150
Pour Point	–11	–9	–40 to –1	2	8	2
Calorific Value (MJ/kg)	18.08	22	42 to 46	39.5	26.65	35.5

approach would not only reduce environmental pollution and dependency on fossil fuels but also create job opportunities. Additionally, future research will explore how to optimize product yields using heterogeneous catalysts, upgrade the biofuel, test different biomass sources for biofuel production, and conduct emission and engine performance testing.

5 Acknowledgement

The authors would like to acknowledge the Khulna University of Engineering & Technology (KUET), Bangladesh, for the financial and logistic support to carry out this work.

References

[1] Sundén, B., 2019. Chapter 1 - Introduction and background. In: Hydrogen, batteries and fuel cells. Academic Press, pp.1-13.

[2] Madureira, N.L., 2014. Key concepts in energy. In: Oil Reserves and Peak Oil. Springer, Cham, pp.101-130.

[3] Asaduzzaman, M., Ali, M.H., Pratik, N.A. and Lubaba, N., 2023. Exhaust heat harvesting of automotive engine using thermoelectric generation technology. Energy Conversion and Management: X, 19, p.100398.

[4] Kader, M., Islam, M., Parveen, M., Haniu, H. and Takai, K., 2013. Pyrolysis decomposition of tamarind seed for alternative fuel. Bioresource Technology, 149, pp.1-7.

[5] Winch, P. and Stepnitz, R., 2011. Peak oil and health in low-and middle-income countries: impacts and potential responses. American Journal of Public Health, 101(9), pp.1607-1614.

[6] Rana, M.M., Al-Mueed, M.M., Islam, M.N. and Ali, M.H., 2025. Production and analysis of biodiesel from mango seed kernels and tamarind seeds using hybrid approach of solvent extraction and transesterification. Results in Engineering, 25, p.103983.

[7] Ali, M.H., Mashud, M., Rubel, M.R. and Ahmad, R.H., 2013. Biodiesel from neem oil as an alternative fuel for diesel engine. Procedia Engineering, 56, pp.625-630.

[8] Bu, Q., Lei, H., Wang, L., Wei, Y., Zhu, L., Zhang, X., Liu, Y., Yadavalli, G. and Tang, J., 2014. Bio-based phenols and fuel production from catalytic microwave pyrolysis of lignin by activated carbons. Bioresource Technology, 162, pp.142-147.

[9] Hossain, M.A., Islam, M.R., Ali, M.H. and Mashud, M., 2013. Emission control of DI diesel engine by using aqueous salt solution. International Journal of Scientific & Engineering Research, 4(6).

[10] Chen, W.H., Peng, J. and Bi, X.T., 2015. A state-of-the-art review of biomass torrefaction, densification and applications. Renewable and Sustainable Energy Reviews, 44, pp.847-866.

[11] Bullo, T.A. and Fana, F.B., 2021. Production and characterization of biodiesel from avocado peel oils using experimental analysis (ANOVA). Journal of Engineering Advancements, 2(2), pp.104-111.

[12] Linus, A.A., Mogaji, T.S., Olabanji, O.M. and Ayodeji, O.Z., 2024. Evaluating the fuel potential of castor biodiesel and its blends for land-based gas turbine engine. Journal of Engineering Advancements, 5(4), pp.107-113.

[13] Demirbas, M.F. and Balat, M., 2006. Recent advances on the production and utilization trends of bio-fuels: a global perspective. Energy Conversion and Management, 47(15-16), pp.2371-2381.

[14] Alam, M.J., Momin, M.A., Ahmed, A., Rahman, R., Alam, K., Islam, A.J. and Ali, M.M., 2017. Production performance of mango in Dinajpur district of Bangladesh (a case study at Sadar Upazilla). European Journal of Agriculture and Forestry Research, 5, pp.16-57.

[15] Geerkens, C.H., Nagel, A., Just, K.M., Miller-Rostek, P., Kammerer, D.R., Schweiggert, R.M. and Carle, R., 2015. Mango pectin quality as influenced by cultivar, ripeness, peel particle size, blanching, drying, and irradiation. Food Hydrocolloids, 51, pp.241-251.

[16] Hasan, K., 2023. DAE predicts record mango production in FY23. [online] Available at: https://businesspostbd.com/back/2023-05-29/dae-predicts-record-mango-production-in-fy23-2023-05-29 [Accessed 20 March 2025].

[17] Amla, B.L. and Potty, V.H., 1985. Development of energy-saving technologies for food processing. Food and Nutrition Bulletin, 7(2), pp.1-8.

[18] Alencar, W.S., Acayanka, E., Lima, E.C., Royer, B., Souza, F.E., Lameira, J. and Alves, C.N., 2012. Application of Mangifera indica (mango) seeds as a biosorbent for removal of Victazol Orange 3R dye from aqueous solution and study of the biosorption mechanism. Chemical Engineering Journal, 209, pp.577-588.

[19] Kittiphoom, S., 2012. Utilization of mango seed. International Food Research Journal, 19(4), pp.1325-1335.

[20] Henrique, M.A., Silvério, H.A., Neto, W.P.F. and Pasquini, D., 2013. Valorization of an agro-industrial waste, mango seed, by the extraction and characterization of its cellulose nanocrystals. Journal of Environmental Management, 121, pp.202-209.

[21] Perea-Moreno, A.-J., Perea-Moreno, M.-Á., Dorado, M.P. and Manzano-Agugliaro, F., 2018. Mango stone properties as biofuel and its potential for reducing CO2 emissions. Journal of Cleaner Production, 190, pp.53-62.

[22] Moyo, M., Pakade, V.E. and Modise, S.J., 2017. Biosorption of lead (II) by chemically modified Mangifera indica seed shells: Adsorbent preparation, characterization and performance assessment. Process Safety and Environmental Protection, 111, pp.40-51.

[23] Demirbas, A., 2009. Potential resources of non-edible oils for biodiesel. Energy Sources, Part B, 4(3), pp.310-314.

[24] Gui, M., Lee, K. and Bhatia, S., 2008. Feasibility of edible oil vs. non-edible oil vs. waste edible oil as biodiesel feedstock. Energy, 33(11), pp.1646-1653.

[25] Chaiyaa, C. and Reubroycharoenb, P., 2013. Production of bio-oil from para rubber seed using pyrolysis process. Energy Procedia, 34, pp.905-911.

[26] Duman, G., Okutucu, C., Ucar, S., Stahl, R. and Yanik, J., 2011. The slow and fast pyrolysis of cherry seed. Bioresource Technology, 102(2), pp.1869-1878.

[27] Shadangi, K.P. and Mohanty, K., 2014. Effect of co-pyrolysis of mahua seed and waste polystyrene on quality of liquid fuel. Journal of Renewable and Sustainable Energy, 6, p.053142.

[28] Larrauri, J., Rupérez, P., Borroto, B. and Saura-Calixto, F., 1996. Mango peels as a new tropical fibre: preparation and characterization. LWT-Food Science and Technology, 29(8), pp.729-733.

[29] Sultana, B. and Ashraf, R., 2019. Mango (Mangifera indica L.) seed oil. In: Fruit Oils: Chemistry and Functionality. Springer, Cham, pp.561-575.

[30] Saka, A., Enkosa, E., Jule, L.T., Nagaprasad, N., Subramanian, K. and Ramaswamy, K., 2022. Biofuel production from mango (Mangifera indica) seed extracts through zinc oxide nanoparticle. Biomass Conversion and Biorefinery, pp.1-11.

[31] Julio, L.G., Aranguren, D.D. and Sierra, R., 2021. Biodiesel synthesis from mango (Mangifera indica) seed oil extracted with supercritical carbon dioxide. In: 29th European Biomass Conference and Exhibition.

[32] Narayanasamy, G., Padmesh, T. and Krishnan, S., 2022. Experimental studies on transesterification of mango (Mangifera indica) seed kernel butter for biodiesel production. IOP Conference Series: Materials Science and Engineering, 1257(1), p.012012.

[33] Ganeshan, G., Shadangi, K.P. and Mohanty, K., 2016. Thermo-chemical conversion of mango seed kernel and shell to value-added products. Journal of Analytical and Applied Pyrolysis, 121, pp.403-408.

[34] Lam, S.S., Liew, R.K., Lim, X.Y., Ani, F.N. and Jusoh, A., 2016. Fruit waste as feedstock for recovery by pyrolysis technique. International Biodeterioration & Biodegradation, 113, pp.325-333.

[35] Lazzari, E., Schena, T., Primaz, C.T., Maciel, G.P., Machado, M.E., Cardoso, C.A.L., Jacques, R.A. and Caramão, E.B., 2016. Production and chromatographic characterization of bio-oil from the pyrolysis of mango seed waste. Industrial Crops and Products, 83, pp.529-536.

[36] Andrade, L.A., Barrozo, M.A.S. and Vieira, L.G.M., 2016. Thermo-chemical behavior and product formation during pyrolysis of mango seed shell. Industrial Crops and Products, 85, pp.174-180.

[37] Ali, M.H. and Moral, M.N.A., 2022. Pyrolytic fuel extraction from tire and tube: Analysis of parameters on product yield. Case Studies in Chemical and Environmental Engineering, 6, p.100273.

[38] Mohammad, I., Abakr, Y., Kabir, F., Yusuf, S., Alshareef, I. and Chin, S., 2015. Pyrolysis of Napier grass in a fixed bed reactor: effect of operating conditions on product yields and characteristics. BioResources, 10(4), pp.6457-6478.

[39] Dyjakon, A., Sobol, Ł., Noszczyk, T. and Mitręga, J., 2022. The impact of torrefaction temperature on the physical-chemical properties of residual exotic fruit (Avocado, Mango, Lychee) seeds. Energies, 15(2), p.612.

[40] Zhang, X., Peterson, C., Reece, D., Haws, R. and Möller, G., 1998. Biodegradability of biodiesel in the aquatic environment. Transactions of the ASAE, 41(5), pp.1423-1430.

[41] Yaman, S., 2004. Pyrolysis of biomass to produce fuels and chemical feedstocks. Energy Conversion and Management, 45(5), pp.651-671.

[42] Pütün, A.E., Apaydın, E. and Pütün, E., 2004. Rice straw as a bio-oil source via pyrolysis and steam pyrolysis. Energy, 29(12-15), pp.2171-2180.

[43] Mashud, M., Ali, M.H., Roknuzzaman, M. and Galib, A.A., 2009. Biodiesel from jatropha oil as an alternative fuel for diesel engine. Proceedings of the International Conference on Mechanical Engineering, Dhaka, Bangladesh.

[44] Venkatachalam, C.D., Sengottian, M., Sivasamy, K.S., Rajadurai, G. and Mani, G., 2020, May. Production of biodiesel from waste cooking oil under varying parametric conditions using hydrodynamic cavitation with a single holed orifice. In AIP Conference Proceedings (Vol. 2240, No. 1). AIP Publishing.

SciEn
Journal of Engineering Advancements Vol. 06(01) 2025, pp 22-30 https://doi.org/10.38032/jea.2025.01.004

Experimental Analysis of Aerodynamic Characteristics of NACA 0012 Wing Model with Multiple Winglets

Md. Zadid Iqbal, Abdullah Al-Faruk, Md. Ashraful Islam*

Department of Mechanical Engineering, Khulna University of Engineering & Technology, Khulna-9203, Bangladesh

Received: March 16, 2025, Revised: March 25, 2025, Accepted: March 27, 2025, Available Online: March 30, 2025

ABSTRACT

Downwash in the wing causes a reduction of lift and generates an additional drag, known as the lift-induced drag or the vortex drag for the finite wing. This induced drag ultimately deteriorates the aerodynamic performance of the aircraft. The technical potentiality of multi-winglets is examined in this work to reduce the induced drag without enlarging the wing's span. Aerodynamic characteristics of the NACA 0012 airfoil section-built wing model with gradual increase of winglets have been studied using a subsonic wind tunnel of 1 m × 1 m × 1 m rectangular test section. An untwisted wing model tapered towered tip was constructed using the NACA 0012 airfoil sections for the wind tunnel experiments. Airfoil-shaped wooden plates of the same airfoil profile were used to make the winglets. Experiments were carried out on the wing with the winglets at 0°, 5°, 10° and 15° incidence angles. The results show that the wing with a gradual increase from one winglet to three winglets can reduce the induced drag and improve the aerodynamic performance. The lift coefficient increases up to 21.2%, and the drag coefficient decreases up to 27.2% when multiple winglets are attached with wing mode compared to single winglet. Enhancing lift performance, reducing vortex drag, and improving overall aerodynamic efficiency in multi-winglet configuration can improve fuel efficiency, leading to better aircraft performance.

Keywords: NACA 0012 Wing, Winglets, Lift-induced Drag, Aerodynamic Characteristics, Wind Tunnel Experiment.

1 Introduction

The most significant lift providing component of an aircraft is the wing. The wing has a streamlined- cross-sectional shape called an airfoil. When the wing moves through the air, the airfoil creates the lift due to the pressure distribution around the airfoil. The average pressure is higher at the airfoil's lower surfaces than that of the upper surface. This pressure difference is the reason for an aerodynamic force whose parallel and perpendicular components for the airfoil chord are defined as lift and drag [1]. When an aircraft moves forward with a velocity, a secondary circulatory motion of air is created around the wingtip because of the pressure difference between the upper and lower surfaces of the wing. This circulatory motion called the wingtip vortices, tends to leak the air from the lower to the upper wing surface, creating a downward velocity component called the downwash [2]. In a typical aircraft design, the wings are attached at their free ends to the fuselage. The outer tips are typically at a higher position than the root tips which make an upward angle with the horizontal plane known as the dihedral. Dihedral is vital for aircraft stability that helps to keep the airplane from rolling accidentally during flight [3]. Wings also carry the fuel for the power plant of the airplane. The mass of the fuel significantly affects instantaneous weight and the airplane's center of gravity.

The designers have created a variety of wings with different aerodynamic properties, mainly based on the subjective purpose and type of the aircraft. For the dispersion of pulverized fluid, the wingtip vortex had been found as an essential factor, and hence the application of agricultural airplanes was introduced. Comparison of several wingtip devices and analysis of the effects on pulverization had been reflected in the work of Coimbra and Catalano [4]. Wingtip devices are usually intended to enhance the aerodynamic efficiency of fixed-wing aircraft. Several types of wingtip devices have been proposed for managing the wake created by the tip vortices in different manners [5]. The wingtip devices can also improve the aircraft's stability characteristics. The wingtip devices are also valued for their aesthetic appeal of the aircraft from a marketing standpoint.

In general aviation, wingtip devices were significant concerns for gliders, which have been researched in primitive ways even though the wings possess a large aspect ratio. Smith et al. [6] mentioned the development work of winglets for sailplanes experimenting on scale models using wind tunnels. It was demonstrated that adding a single winglet onto the biplanes increased the lift-curve slope and the maximum lift coefficient and calculated a 13% improvement in the vehicle's endurance. Kroo et al. [7] dealt with winglets in a wider concept of non-planar wings. In that study, different types of wings, like box wings, nag wings, etc., were reviewed along with non-planar wakes wings exploited in general. A key constraint in design interest for many aircraft is the potentiality for lowering the vortex drag without increasing the span. Yates and Donald [8] concluded that for small transporter airplanes, single winglets are advantageous; they provide 10% lower induced drag compared to the plain wing of elliptical shape. Ismail et al. [9] conducted an experimental study to measure the effect of the angle of attack on the NACA 4415 wing and found that the wing is more efficient at a lower speed than a higher speed. Al-Atabi [10] investigated devices akin to the wing tip airfoils, named "wing tip sails", on the wingtip fuel tank of a trainer aircraft for fuel use. After the wind tunnel testing of such sails up to four, the reduction of fuel consumption between 3.5% and 5% was demonstrated and confirmed by the flight test experiments. An experimental and numerical investigation by Eftekhari and Al-Obaidi [11] on the finite wing at low Reynold's number established that the drag force acting on the airfoil increases with the increase of incidence angle due to the change of laminar to

*Corresponding Author Email Address: alfaruk@me.kuet.ac.bd Published by: SciEn Publishing Group

turbulent flow. Cerón-Muñoz and Catalano [12] experimented on the adaptive multi-winglets through variation of winglet cant angle and showed a decrease in wake turbulence from the winglets in the wing. They concluded that the symmetrically designed winglets were the best for general aviation aircraft and less effective on the tapered wings.

Aerodynamic characteristics for the wing model of the NACA 4315 section without and with winglets of rectangular, triangular, and circular type had been investigated experimentally in a subsonic wind tunnel by Inam et al. [13]. They suggested that the triangular winglet at 5° inclination has the best performance providing a 30.9% reduction in drag compared to other configurations for the maximum Reynolds number considered. The effect of the cant angle of blended type winglet are numerically studied on the aerodynamic characteristics and compared the performance with the plane wing without winglet of the same wing model [14], [15]. It has been concluded that 90° cant-angled winglets exhibit the best performance in terms of lift coefficient, drag coefficient, lift-to-drag ratio, and stall angle of attack compared to other cant-angled winglet models and the plain wing without winglet. Yusoff et al. [16] investigated the evolution of induced drag in Unmanned Aerial Vehicles (UAVs) for a fixed Reynolds number utilizing up to seven winglets arranging them in different cant angle on NACA 23015 profile. The study demonstrated better aerodynamic characteristics at low angle of attack through the reduction of induced drag. Reddy et al. [17] numerically studied a multi-objective optimization of aerodynamic shape for wing-tail-body aircraft configuration consisting of 33 parameters using modelFRONTIER for four simultaneous objectives. The study concluded that Pareto-optimized multi-element winglet demonstrated better performance at high-speed flight regime of subsonic and transonic speeds. Padmanathan et al. [18] conducted a parametric optimization study on novel winglet designs such as, multi-tip, bird-type, twisted etc. for transonic aircraft. The numerical study compared the optimized winglet design with the baseline model (NASA common research model) and reported 18.29% improvement in aerodynamic efficiency by Taguchi method and that of 20.77% by T-GRA coupled with the PCA method. Bio-inspired wing tip devices are numerically investigated by Sethunathan et al. [19] aiming to reduce the wing-tip vortices at low and medium-range Reynolds numbers. The study incorporates three- and four-tipped multiple winglets by making different combinations through varying the cant angle of each tip and reported 22-23% increase in aerodynamic efficiency and better stability compared to straight wing. Bala et al. [20] computationally examined the flow field over a transonic wing which incorporates four different winglet model based on the cant angle and analyzed the pressure variation along with coefficients relevant of wing model.

Moreover, a wing with multiple winglets has the potential to give some other benefits. Having two or multiple winglets in the wing reduces the climb thrust. A winglet-equipped aircraft can typically take a 3% increase in the lift coefficient over the non-winglet equivalent aircraft. This can extend engine life and reduce maintenance costs [21]. If no or single winglets form a wing, it increases cruise thrust. Cruise fuel flow is reduced by up to 6%, saving fuel costs and increasing range. It also improves cruise performance. Winglets can allow aircraft to reach higher levels sooner [22]. Ulrich et al. [23] employed WINGGRID devices experimentally for the reduction of induced drag. The study concluded that multiple winglets can reduce induced drag by approximately 20% using multiple winglets. As wings with multiple winglets improve fuel efficiency, the noise effects can be significantly reduced due to vortex effects [24]. Consequently, it also reduces carbon emissions. It surely can be advantageous and helpful in air traffic control as it reduces cyclone-type effect/turbulence [25]. However, the appearance has been better than the typical winglet design. Winglets bring a modern look and feel to aircraft and improve customers' perceptions of the airline.

Appraising the literature mentioned above, it is demonstrated that aircraft of any type with winglets attached to the wing have aerodynamically better performance than those without winglets. Previous studies examined multiple winglets of different types at different orientation on the diverge arrangements with fixed or moveable wings which are mostly conducted through numerical approach. However, there are lack of experimental investigations. Moreover, no studied are found that take the NACA 0012 profile for both the wing and winglet in experimental research. In this experimental work, NACA 0012 wing model has been investigated that is attached in a near perpendicular plane with a streamlined, airfoil-shaped plate at the outer tip as winglet and then gradually increased the number of winglets up to three. The winglets were placed side by side at the tip, and additional winglets were slightly canted outward from the fuselage. Aerodynamic characteristics for the wing model with a gradual increase of winglets have been compared and presented. Reynolds number dependence on the aerodynamic performance is examined for varying the angle of attack in this work.

2 Wing Model Description and Construction

This study uses a symmetric NACA 0012 airfoil section to make the finite wing. The equation of thickness distribution for a symmetrical 4-digit NACA airfoil is given by

$$y_t = 5t\left[0.2969\sqrt{\frac{x}{c}} - 0.1260\left(\frac{x}{c}\right) - 0.3516\left(\frac{x}{c}\right)^2 + 0.2843(x/c)^3 - 0.1015(x/c)^4\right] \quad (1)$$

The leading edge of the airfoil approximates a cylinder whose radius can be expressed as

$$r_t = 1.1019ct^2 \quad (2)$$

where c is the chord length of the airfoil, x is the position along the chord from the leading edge to the trailing edge, and t is the maximum thickness as a fraction of the chord [3]. The thickness y_t does not tend to zero from the above equation at the trailing edge of the airfoil $(x/c) = 1$). For computational analysis where zero-thickness may be required, a method can be established with modification of any coefficient to make the sum zero. The last coefficient in Eq. (1) can be revised to -0.1036, which slightly changes the overall airfoil shape. The coordinates (x_u, y_u) of the upper airfoil surface, and (x_l, y_l) of the lower airfoil surfaces were computed using the equation [2]:

$$x_u = x_l = x \;;\; y_u = +y_t \;;\; y_l = -y_t \quad (3)$$

A NACA 0012 airfoil is selected, designed, and constructed for the present study. The last two digits (00 in the present case) indicate that it is symmetrical; there is no camber at all and 12 indicates that the airfoil is 12% as thick as it is long, which means it has a maximum thickness of 12% to the chord length.

The structured surface profile of the NACA 0012 wing model was developed using SOLIDWORKS software, as shown in Fig. 1.

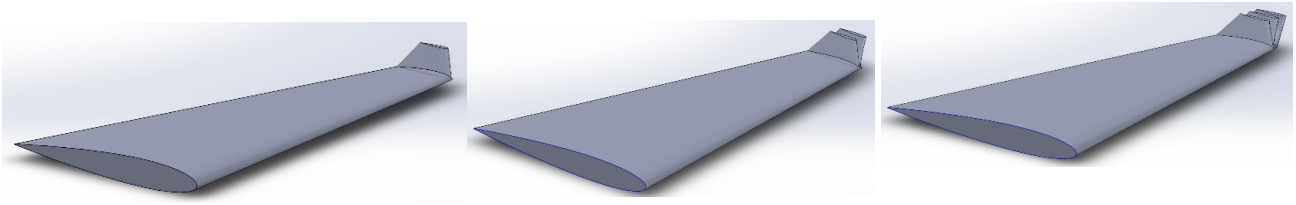

Fig. 1 Wing model of an airplane with one winglet (left), two winglets (middle) and three winglets (right) developed in SOLIDWORKS

To maintain the perfect aspect ratio of chord length to the span of wing, the designed model was printed. It also provides a way to visualize the wing model before the actual construction of it. The wing model was constructed with no geometric and aerodynamic twists to keep things simple so that their effect may be neglected, as shown in Fig. 2. The material used to construct the wing is "Sirish Wood", whose scientific name is "Albizia saman".

The whole section was made in the woodshop and machine shop of KUET, Khulna. Some wood pieces of required cross sections were taken in the woodshop. Each airfoil section was made very carefully with a soft hand to maintain good accuracy. The wingspan was limited to 30 cm without any sweep. The maximum chord length was 20 cm at the root side, while the minimum was 6 cm at the wing's tip side, making a taper ratio of 0.3. The determination of the average chord length of the wing model was necessary to have the Reynolds number of the same order. Because the exploration of wingtip vortices formation had been a major concern, the Reynolds number based on the average chord length is relevant at low flight speeds. In this sense, the Reynolds number was estimated to be about 10^5 in this work. The aspect ratio of the wing signifying the span length relative to the chord length is one of the critical design parameters for the finite wing. The relative weight of the model could be reduced by making it as large as possible.

Fig. 2 Constructed wooden aircraft wing model with three winglets for the experiment in the wind tunnel

The airfoil was drilled with the help of a 1.5 mm diameter drill bit from the wing tip after 1 cm apart from the leading edge to the trailing edge. At the mid-section, a reference point was marked as the center of the winglet. Then the pressure taping points were drilled at a distance of 2 cm on both sides from the marked reference center. The pressure tapping points on the measuring surfaces were numbered sequentially to track the serial. Then the venial pipes were attached to each of the pressure tapping points. The winglets were not fixed to the wing at the very beginning. At first, one winglet was attached to the wing. It was necessary because an actual size and shape should be checked for one winglet rather than three. The concept was to find the error of construction, if any. The tips of the winglets were made as sharp as possible because there was no curve or round tip was necessary for the present study.

After constructing the wing, the winglets were constructed using the same material and process. The winglets are basically a wing having airfoil shape cross-section that extend from the tip of the wing. However, instead of laying on the same plane of wing, the winglets are non-coplanar structure attached at a certain angle with the plane of the wing at the tip. At first, a single winglet is attached with the main wing body. Subsequently the second and third winglets are attached to the first winglet as presented in Fig. 2. Now the wing with the winglets is ready for testing and to measure the pressures in the wind tunnel. After recording the data, two winglets are attached to the existing one and repeat the procedure to compare the aerodynamic characteristics with the previous one. Afterwards another winglet is attached to the existing two, and so on. The winglets are attached to the wing at the tip.

3 Experimental Setup and Procedure

The experimental tests of the study were conducted in the Aerodynamics and Aerial Robotics Laboratory of the Mechanical Engineering Department at Khulna University of Engineering & Technology, Khulna. The laboratory has locally designed and constructed wind tunnel which consists of a subsonic wind tunnel of 1 m × 1 m rectangular test section [26]. The wind tunnel's operational speed limit of airflow can be up to 42 m/s. The turntable of the wind tunnel where the wing models were fitted could set an angle of attack up to 45°. To address the concern of violating the Reynolds number analogy requirements, the aerodynamic characteristics of a large wing model are inspected. A large wind tunnel facility is necessary; therefore, the wing model must be appropriately scaled down to match the usual wind tunnel size. Moreover, there are some limitations in wind tunnel experiments that should be considered; it would be difficult to support the wing model at a desirable height. The size of the wing models was selected so that they could be fitted in the test section of the wind tunnel for the full range of angles of attack.

At the time of constructing the actual model of the section of the wing, an observation was first made about its length compared to the vacant space of the test section. The design created in the software is almost similar when constructing the model in real. The tapping points for pressure tubes were measured. The points were not drilled from the edge of the winglet; a 2 cm gap was maintained. The reason is that the peak value of the lift and drag coefficient will be found at a distance from the trailing edge.

Since the lifting force is necessary to sustain the load of the wing model, placing the constructed model in the test section of the wind tunnel at the beginning of the experiment is crucial. The respective wing models were mounted on the turntable of the wind tunnel test section with the help of a frame. The pressure measuring sensors were the primary instruments for acquiring the test data. The pressure measuring sensors were inserted at

different pre-drilled points from leading to trailing edges, as shown in Fig. 3. Before conducting experiments, precautions were taken, *e.g.*, checking and fixing the specimen model twice before switching ON the wind tunnel and closing the wind tunnel's opening section.

Fig. 3 The wing model placed in the test section of the wind tunnel [26] and pressure tubes are inserted to measure the static pressures

The Bernoulli's principle explains how the energy is conserved between two points of a fluid flow if there is no forced change. This principle was used to determine air velocity in the throat section of the wind tunnel. The airfoil design is symmetrical, so the pressure distribution was desired to be symmetrical on the upper and lower surfaces at zero wing incidences. Using pressure tubes, the pressures on the upper and lower surfaces were measured to ascertain the zero incidences of the wing. The pressures were actively responsive to the change in the angle of attack. To replicate this theoretical change into a practical one for every angle of attack of the airfoil, the pressures were measured. For 0°, 5°, 10°, 15° angles of attack, the respective pressures were determined in the condition of room temperature. There was a limitation of attaching the number of pressure tubes simultaneously, so five pressure taping points were initially attached to the pressure measuring sensor to the upper surface. After that, with the help of Lab View software, the values of the surface pressures of the airfoil were determined.

The constructed wing of the NACA 0012 section with only one winglet was mounted inside the wind tunnel's test section frame. The testing section began at the first step after setting the angle of attack 0° measurement. The experiment was carried out for different velocities; the pressures were measured simultaneously. Then, the angle of attack was changed to 5°. To examine the changes and compare the differences, the lift and drag forces were measured along with pressure from the relative scales for different velocities. Next, the angles of attack were changed to measure the necessary data in the same way stated before.

A regulator was attached to the wind tunnel by which the velocity of the wind tunnel was controlled. The performed value was taken into 300 volts of the wind tunnel in relation to the room temperature. Barometer recordings showed the ambient pressure, whereas humidity and temperature were determined by a hygrometer and thermometer, respectively, to evaluate air density in the laboratory environment. The tests were carried out with a free-stream velocity of 29.24 m/sec, 34.29 m/sec, and 39.15 m/sec for the respective Reynolds number. For the angle mentioned above of attacks with the help of a pressure sensor, the wing's upper and lower surface pressures were measured. Multiple winglets, i.e., two and then three winglets, were used, and those were triangular. The triangular winglets were attached to the wing at the wingtip. To tackle the issues of experimental uncertainty and repeatability of test data, considerable attention and precautions are taken during the wind tunnel testing so that confidence can be placed on the results. All the testing were conducted in controlled environment so that the airflow, temperature, and pressure variations are limited in the test section [27].

After measuring the necessary data needed, the calculation process was started. The pressure coefficients on the upper and lower surfaces were calculated from the measured pressure, and the lift coefficient and drag coefficient were calculated using the mathematical relationship of the coefficient of pressure:

$$C_p = \frac{p - p_\infty}{q_\infty} = \frac{p - p_\infty}{\frac{1}{2}\rho_\infty {V_\infty}^2} \tag{4}$$

where p is the local static pressure, p_∞ is freestream pressure, V_∞ is the free stream velocity, and ρ_∞ is the free stream density corresponding to the freestream pressure.

From the equation, the value of the C_p is found, and lift and drag coefficients are calculated by integrating the pressure coefficient over the wing. That is, the coefficient of lift

$$C_L = \frac{1}{c}\int_0^c \left(C_{p,l} - C_{p,u} \right) dx \tag{5}$$

and coefficient of drag

$$C_D = \frac{1}{c}\int_0^c \left(C_{p,u}\frac{dy_u}{dx} - C_{p,l}\frac{dy_l}{dx} \right) dx \tag{6}$$

where c is the chord length, $C_{p,l}$ is the pressure coefficient at the lower surface and $C_{p,u}$ is the pressure coefficient at the upper surface [3].

4 Results and Discussion

All the necessary measurements of wind tunnel deploying the constructed aircraft wings with a gradual increase of winglets were conducted. The lift and drag coefficients have been calculated from the experimental pressure coefficient data using Eqs. (4) to (6). Different plots of performance parameters have been drawn to examine the measured data and the calculated results. The coefficients of lift and drag depend on airstream velocity, platform area, profile shape of the airfoil, angle of attack, and angle of winglet (considering the initial position perpendicular with wing). The first two factors determine the dynamic pressure of the airstream. The last three factors mentioned above influence how much drag will be developed in relation to the angle of attack. Therefore, all these factors greatly instigate the coefficient of lift and drag coefficients.

To assess the conditions and conclude the results, systematic analyses are made with the idea of comparing the pressure coefficients against the percentage of chord length for the gradual increase of winglets. It means at first one winglet was considered; next two winglets and three winglets were considered. Three Reynolds numbers were taken randomly, which were calculated based on the free stream velocity at the wind test section. The percentage of chord length was taken up to 100; the interval between them was 10 and started from 0. In the experimental setup, the angles of attack were fixed at 0°, 5°, 10°, 15°. The characteristics of pressure coefficients of the aircraft wing model under test at 0° angle of attack for different Reynolds number are shown in Fig. 4.

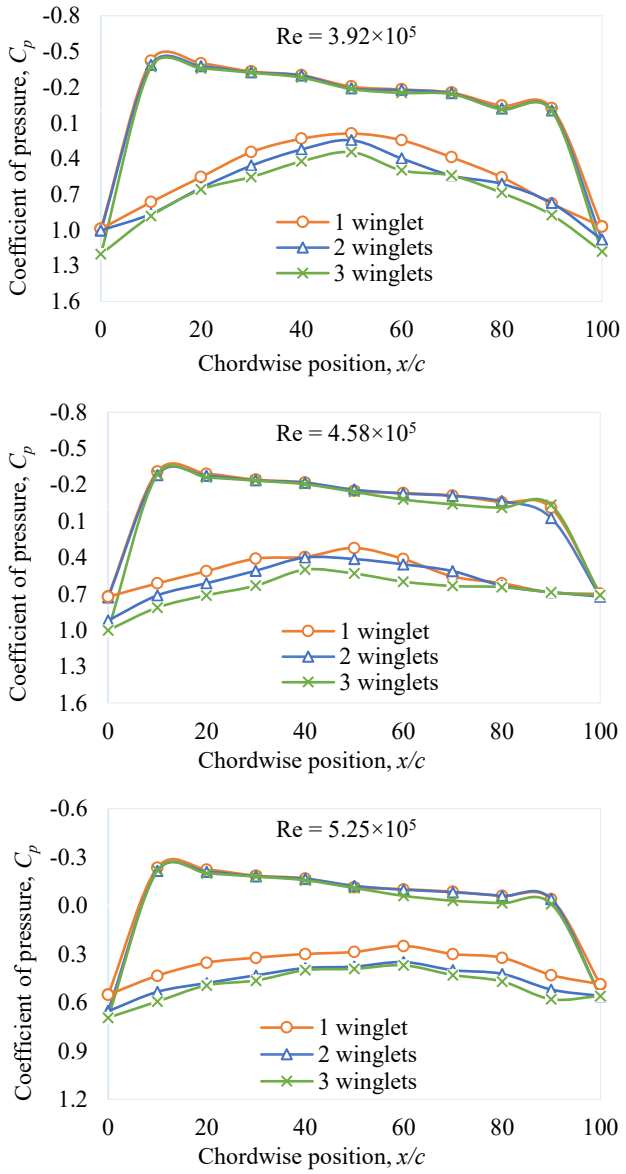

Fig. 4 Distribution of pressure coefficients against the percentage of chord length for different number of winglets and different Reynolds numbers at 0° angle of attack

The plots showed that for the subsequent downstream positions along the chord of the wing, the pressure coefficient reached a certain maximum point (absolute value) for all the three winglet configurations. Just downstream of the leading edge nearly at $x/c = 20$, the peak point was observed for the upper surfaces of winglets and then gradually it began to go downward. For the lower surfaces, the peak points are achieved nearly at 50 percent of the chord length. Similar characteristics were monitored for other Reynolds number shown in Fig. 4. The graphs demonstrated that the C_p at the leading and trailing edges are the same for both the upper and lower surfaces because these points are essentially the same location at 0° angle of attack where the wing model perfectly placed horizontal. It can also be noticed that the two stagnations points at the leading and trailing edges showed the highest C_p at these positions for all the Reynolds numbers.

The comparison of pressure coefficients at the percentage of chord length positions for the periodic increment of winglets has been illustrated in Fig. 5 for different Reynolds number at 5° angles of attack.

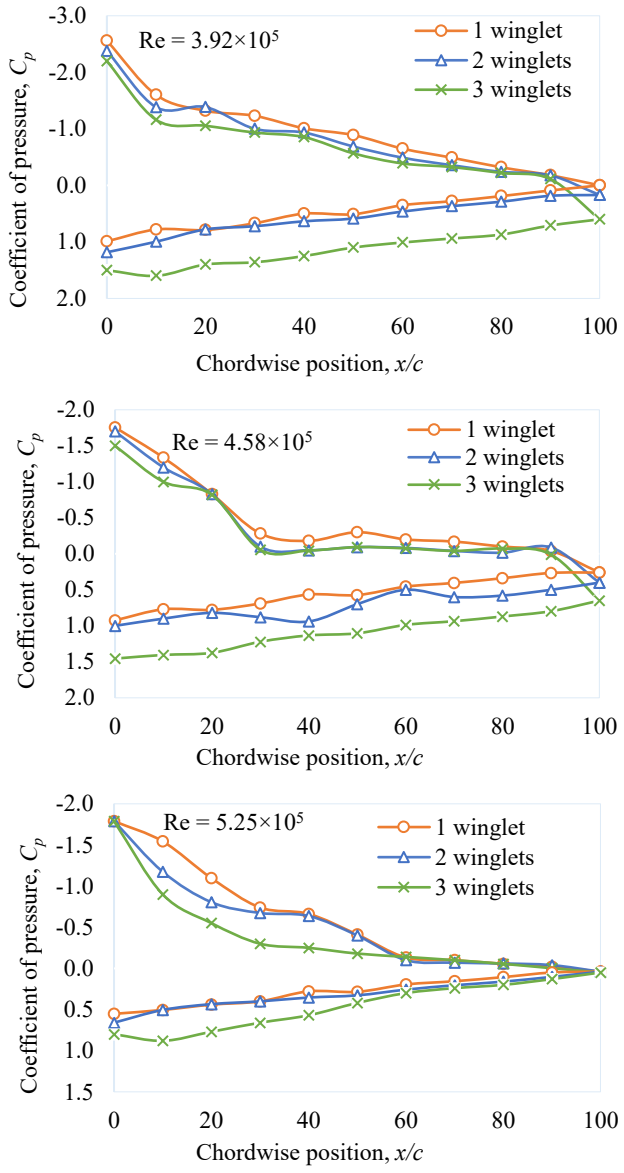

Fig. 5 Variation of pressure coefficients over wing surfaces versus the percentage of chord length for the gradual increase of winglets at 5° angle of attack for various Reynolds numbers

Though the line curves for upper and lower pressure coefficients contrast in their moving in different directions, the major indication is that for a 5° angle of attack, the curve for three winglets is the least one on both occasions. In contrast, the higher values for one winglet gives the elevated C_p curves for both upper and lower surfaces. Comparing to the C_p curves at the 0° angle of attack, the value pressure coefficients increased significantly because of higher angle of attack for all three cases of Reynolds number. The pressure coefficient at the upper and lower surfaces near the leading edge are now different value at 5° angle of attack because it is tilted up from the initial horizontal positions at 0°. However, the values at the trailing edge remain the same since trailing edge is very sharp compared to the rounded leading edge of NACA 0012 airfoil.

To identify the variation of the C_p curves at higher angle of attack, the experiment was carried out with a 10° angle of attack as presented in Fig. 6 for the three Reynolds numbers investigated. The curves have shown look alike characteristics compared to the curves at 5° angle of attack.

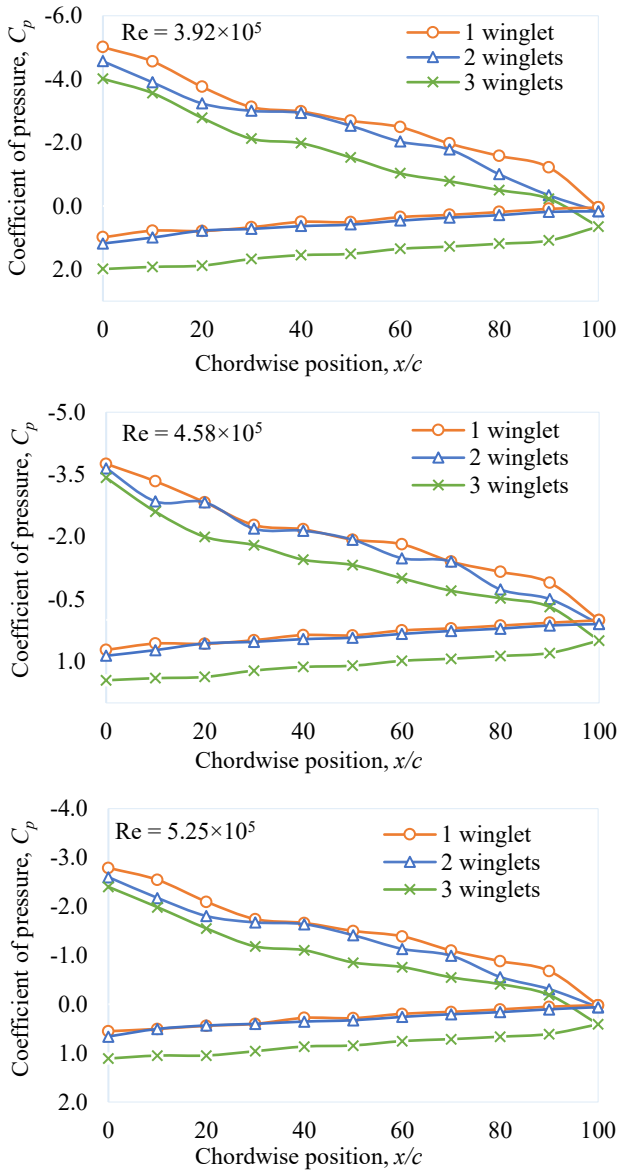

Fig. 6 Comparison of pressure coefficients vs percentage of chord length for the gradual increase of winglets ($Re = 3.92\times10^5$ and 10° angle of attack)

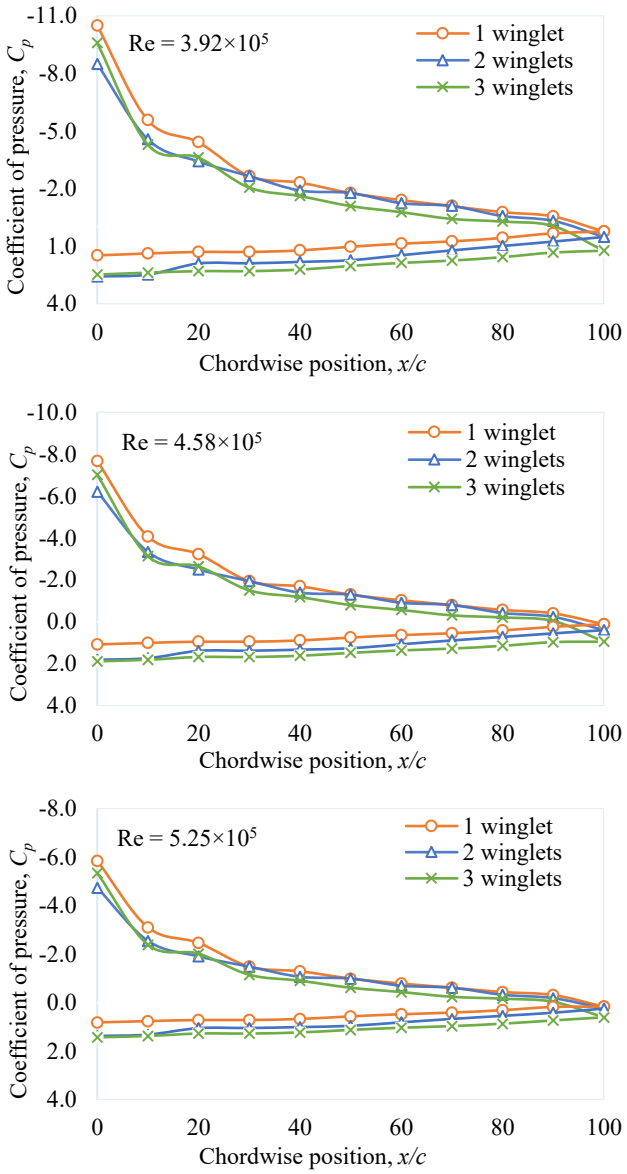

Fig. 7 Pressure distribution comparison on the upper and lower surfaces in different chord positions of wing model for the single and multi-winglets configuration at 15° angle of attack for various Reynolds number

However, the C_p values at the upper surfaces increased much compared to the respective values at 5° incidence positions for all Re cases. The values at the lower surfaces not changed greatly indicating the similar pressure distribution between the two angle of attack positions. The curves for the lower surface of the wing are nearly intersected at every point for single and double winglets.

However, for the three winglets, there is a clear distinction with the other two curves for both the upper and lower sides of the winglets.

Again, the pressure coefficients in Fig. 7 suggested that for the 15° angle of attack and the different Reynolds numbers, the coefficients give an elevated curve for one winglet. In contrast, the bottom one has been a standstill for the case of three. The middle curve is the wing containing three winglets for both the upper and lower positions. Observing the C_p curves in Fig. 4 to Fig. 7 for all the angle of attack ranging 0-15° demonstrated that increasing the Reynolds number decreases the pressure coefficients specially at the upper surface.

Keeping in mind that the lift generated in a wing is the net difference between the upper and lower surface pressure; the above trend suggest that higher flight velocities generate less lift coefficient.

The characteristics of pressure coefficients of the wing model at 5°, 10°, and 15° angles of attack are shown in Fig. 5, Fig. 6, and Fig. 7, respectively. The curves showed very similar characteristics for both upper and lower surfaces. However, the pressure coefficient of the upper surfaces begins from a certain maximum point for all three winglets and then gradually goes downward. Therefore, with the increase of the angle of attack, the peak point of the pressure coefficient on the upper surface is shifting towards the leading edge. On the other hand, the peak points are achieved nearly at 100 percent of chord length for the lower surfaces. Gradual increase of pressure coefficient for the lower surface had been increasing with the percentage of chord length. After consulting the characteristics of pressure coefficient plots of Fig. 5, Fig. 6, and Fig. 7, suggests that for 0°, 5°, 10°, 15° angle of attack and all the considered Reynolds

numbers, the coefficient of lift may be calculated to have a higher value when the wing consists of three winglets rather than one or two. The above results could conclude that using three winglets in a wing is more effective because the pressure difference is more than the other two for all three Reynolds numbers.

After analyzing the pressure distributions through the pressure coefficient plots, the average pressure coefficients are calculated for different angles of attack at Re value of 5.25×10^5, and plotting them in a graph as displayed in Fig. 8.

After analyzing the curves, it can be said that a stable and similar nature was shown for a range angle of attack starting from 0° up to 15°. The average pressure coefficient is decreasing in upper surface and that of the lower surface is increasing making the difference between the two surfaces diverging for all the winglet configurations. This suggest that lift increases at higher angle of attack positions. However, some deviation could be seen for the three different numbers of winglet arrangements. For three winglets arrangement, the curves are lowest for both the upper and lower surfaces of the wing. A decisive statement could be drawn from this those changes in the curves that the increment of the angle of attack increases the net change of average pressure coefficients, consequently increasing the lift coefficient.

Another approach was taken to compare the effects of Reynold's number on average pressure coefficients. The average pressure coefficient for the upper and lower surfaces at 5° angle of attack are plotted against the Reynolds numbers in Fig. 9. The figure illustrates a contrasting pattern for the upper and lower curves for all three different configurations of winglets. However, the curve for three winglets is the bottom one for the lower surface, while for the upper surface, the higher curve is for three winglets. Hence, with the increase of Reynold's number, the average pressure coefficient for the upper surface is decreases, whereas the gradual increment could be seen for the lower one with the increment of Reynold's number. The plots clearly demonstrating that increasing the Re decreases the net difference between of average C_p, reduces the lift at higher values of Re.

The main objective was to calculate the lift and drag coefficients from the pressure coefficients. The lift coefficient can be said as "the ratio between the lift force and the product of dynamic pressure and area". It is one of the measures of the effectiveness of airfoil to produce lift.

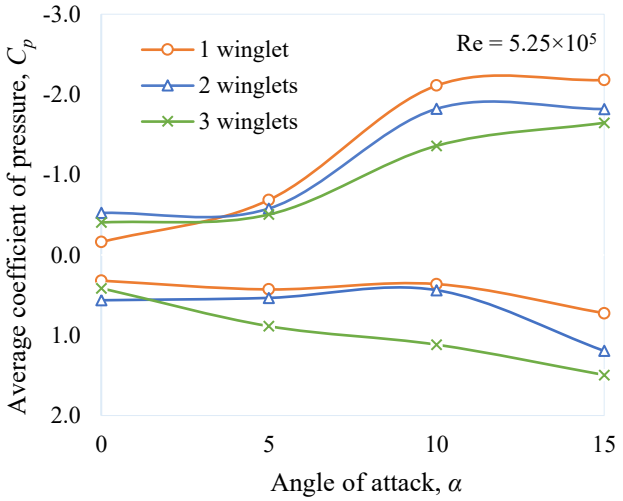

Fig. 8 Average pressure coefficients vs angle of attack for the gradual increase of winglets

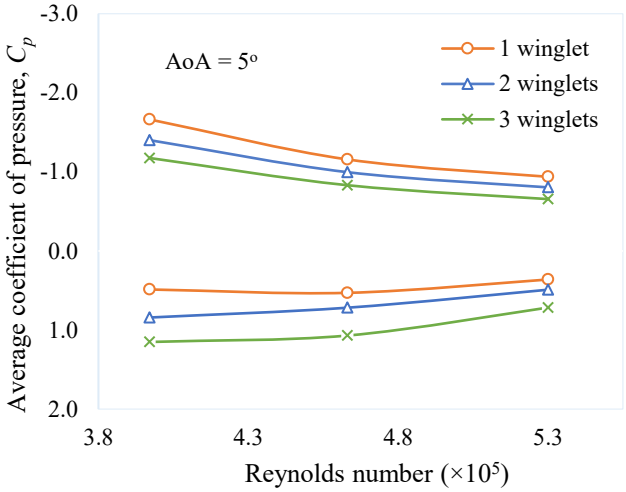

Fig. 9 Average pressure coefficients vs Reynolds number for the gradual increase of winglets

The values of lift coefficients varying with different angles of attack have been obtained from experimental data. The importance of the angle of attack in determining wing performance cannot be overemphasized. The lift characteristic is also dependent upon or affected by thickness distribution and location of maximum thickness, camber, and other factors such as increasing the thickness, which results in lower static pressure and more lift.

The lift coefficient variation with angle of attack at 5.25×10^5 Reynolds number was represented in Fig. 10. Observing the curves for one, two, and three winglets indicate a better lift coefficient when three winglets were attached with the main wing body for different angles of attack. The maximum lift coefficient of 1.97 was obtained near 10° angle of attack for three winglets arrangement. After that, all three curves are declining indication stalling of the wing that occurred because of the flow separation on the upper surface of wing. In Fig. 11, the drag coefficient for the incremental angle of attack for the arrangements at 5.25×10^5 Reynolds number is presented. The curves clearly showing that increasing the angle of attack increasing the drag coefficients for all the cases because of higher pressure drag on the wing models. The pressure drag on the wing increases with the increase of angle of attack due to its shift from the streamlined position at 0° incidence with respect to freestream direction.

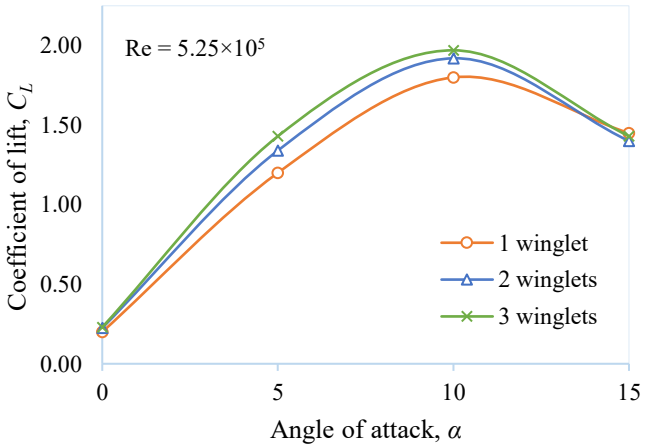

Fig. 10 Variation of lift coefficient with angle of attack for the multi-winglet configurations at Re = 5.25×10^5

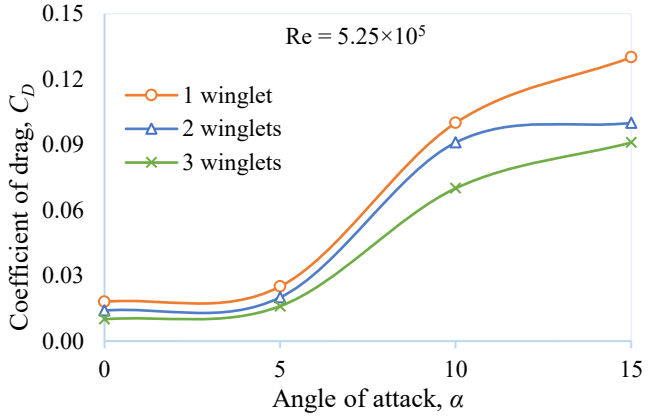

Fig. 11 Variation of drag coefficient with angle of attack for the multi-winglet configurations at Re = 5.25× 10^5

The C_D values for one winglet are higher than the other two conditions. Moreover, the drag coefficients are lower for three winglets arrangement. It is a diligent way of reflecting on the advantages of three winglets. However, skin friction drag may occur, but induced drag is the primary factor contributing more to drag formation in winglets. This is why adding more winglets after using three, could have obtained lower values.

Lift-to-drag ratio is another significant tool to evaluate the performance of a wing with single or multi-winglets. Computational research work showed that multi-winglets could yield significant reductions of induced drag in the lower two-digit percentage range compared to planar wing concepts having the same wing area and span [28]. The lift-to-drag ratio for different angles of attack is presented in Fig. 12 at Re = 5.25× 10^5. From the figure, it is seen that the ratio of lift to drag is higher at the beginning of the angle of attack for two winglets, but as the angle of attack, the value of lift to drag ratio rises for three winglets. However, a peak value has been obtained around 5° angle of attack. This behavior is because when the angle of attack is increased until the lift-to-drag ratio reaches its maximum value, both C_L and C_D increase, but C_L increases more than C_D. The maximum lift-to-drag ratios for one-, two-, and three-winglets configurations are found to 48, 67, 89, respectively, at 5° angle of attack for all cases. As the lift-to-drag ratio is considered as the aerodynamics efficiency of an aircraft, this value of 5° AoA can be taken as the cruise angle of attack in the multi-winglet configuration. This finding of the study is consistent with the findings of literature [2].

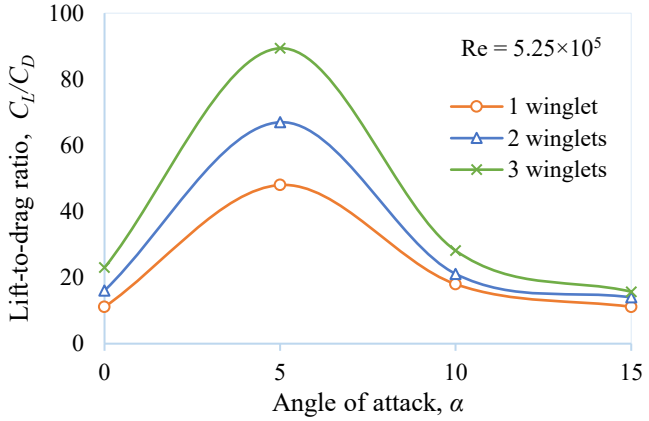

Fig. 12 Variation of lift-to-drag ratio with the angle of attack for the multi-winglet configurations at Re = 5.25× 10^5

5 Conclusions

It has long been theoretically stamped that winglet can be a phenomenal addition in the wing to reduce the induced drag. However, the actual performance of technical adaptations of multi-winglet configurations often fell short of the expectations raised by the theoretical predictions. The experimental data from this work confirmed the improvements in aerodynamic coefficients by using multi-winglets. The pressure distribution on the surfaces of the wing varies to the angle of attack and Reynolds number considerably. The maximum lift producing point (minimum pressure point) on the upper surface moves towards the leading edge from the percentage of chord position of 20% at 0° with the increase of angle of attack. It is depicted from the drag and lift coefficient graphs that the use of multiple winglets increases the lift coefficient and reduces the drag coefficient. The experimental results also showed that the wing with a gradual increase of winglets can reduce the induced drag and improve the value considerably compared with the wing without winglets. For all cases, a wing with one winglet showed less advantages than the two or three-winglet configurations. In particular, the pressure coefficients for lower and upper surfaces indicated that a wing with three winglets provides a better lift coefficient and reduces drag coefficient. Accordingly, three winglets provide more benefits as the results suggested. From all the points of view, multiple winglets are advantageous over single or no winglets in the wing. It is expected that shape of the winglet and appropriate selection of the geometrical parameters of the winglet may further improve the aerodynamic performance of the wing which can be investigated both numerically and experimentally in the future.

Nomenclature

c	Chord length (m)
C_D	Coefficient of drag (-)
C_L	Coefficient of lift (-)
c_p	Coefficient of pressure (-)
p	Actual pressure of the body (N/m^2)
p_∞	Free stream pressure (N/m^2)
S	Wing surface area (m^2)
t	Maximum thickness (m)
V_∞	Free stream velocity (m/sec)
α	Angle of attack (degree)
μ_∞	Free stream viscosity (kg/m.sec)
ρ_∞	Free stream density (kg/m^3)
AoA	Angle of attack (degree)
Re	Reynolds number (-)

Acknowledgments

The authors warmly recognize the wind tunnel testing facilities at the Department of Mechanical Engineering, KUET, Bangladesh. The authors are indebted to Md. Mushfiqur Rahman of KUET for helping in the CAD modeling of the wing model.

Conflict of Interest

There is no known conflict of interest associated with this publication and there has been no significant financial support for this work that could have influenced its outcome.

References

[1] Khan, M.M.I. and Al-Faruk, A., 2018. Comparative analysis of aerodynamic characteristics of rectangular and curved leading edge wing planforms. *American Journal*

of Engineering Research (AJER), 7(5), pp.281-291. Available at: <www.ajer.org>.

[2] Anderson, J.D. Jr., 2011. *Fundamentals of aerodynamics.* 5th ed. New York: McGraw-Hill.

[3] Houghton, E.L., Carpenter, P.W., Collicott, S.H. and Valentine, D.T., 2017. *Aerodynamics for engineering students.* 7th ed. Oxford: Butterworth-Heinemann.

[4] Coimbra, R.F.F. and Catalano, F.M., 1999. Estudo experimental sobre pontas de asa para uma aeronave agrícola. *Revista Brasileira de Engenharia Agrícola e Ambiental, 3*(1), pp.99-105.

[5] Krishnan, S.G., Ishak, M.H., Nasirudin, M.A. and Ismail, F., 2020. Investigation of aerodynamic characteristics of a wing model with RGV winglet. *Journal of Aerospace Technology and Management, 12, e2020.*

[6] Smith, M., Komerath, N., Ames, R., Wong, O. and Pearson, J., 2001. Performance analysis of a wing with multiple winglets. *19th AIAA Applied Aerodynamics Conference.* Reston, Virginia: American Institute of Aeronautics and Astronautics. doi:10.2514/6.2001-2407.

[7] Kroo, I., McMasters, J. and Smith, S.C., 1996. Highly nonplanar lifting systems. *Transportation Beyond 2000: Technologies Needed for Engineering Design.*

[8] Yates, J.E. and Donaldson, C.D., 1986. A fundamental study of drag and an assessment of conventional drag-due-to-lift reduction devices, *NASA Technical Report*, NASA-CR-180891.

[9] Ismail, N., Usman, K.M., Balogun, M.B., Abdullahi, M., Faru, F.T. and Ibrahim, I., 2020. Effect of angle of attack on lift, drag, pitching moment and pressure distribution of NACA 4415 wing. *Journal of Science Technology and Education, 8*(1), pp.31-44.

[10] Al-Atabi, M., 2006. Aerodynamics of wing tip sails. *Journal of Engineering Science and Technology, 1*(1), pp.89-98.

[11] Eftekhari, S. and Al-Obaidi, A.S.M., 2019. Investigation of a NACA0012 finite wing aerodynamics at low Reynold's numbers and 0o to 90o angle of attack. *Journal of Aerospace Technology and Management, 11, e1519.*

[12] Cerón-Muñoz, H.D. and Catalano, F.M., 2006. Experimental analysis of the aerodynamic characteristics adaptive of multi-winglets. *Proceedings of the Institution of Mechanical Engineers, Part G: Journal of Aerospace Engineering, 220*(3), pp.209-215.

[13] Inam, M.I., Mashud, M., Al-Nahian, A. and Selim, S.M.S., 2010. Induced drag reduction for modern aircraft without increasing the span of the wing by using winglet. *International Journal of Mechanical & Mechatronics Engineering IJMME-IJENS, 10*(3), pp.49-53.

[14] Sayem, M.S.H., Sagar, M.M., Alam, R. and Al-Faruk, A., 2024. Numerical analysis of aerodynamic characteristics of aeroplane wing with winglets. *International Research Journal of Engineering and Technology, 11*(5), pp.1601-1622.

[15] Sayem, M.S.H. and Al-Faruk, A., 2020. Effect of cant angles on the aerodynamic performances of an airplane wing with blended type winglet: Numerical analysis. *International Conference on Mechanical, Industrial and Energy Engineering.* Khulna.

[16] Yusoff, H. et al., 2022. The evolution of induced drag of multi-winglets for aerodynamic performance of NACA23015. *Journal of Advanced Research in Fluid Mechanics and Thermal Sciences, 93*(2), pp.100-110. doi:10.37934/arfmts.93.2.100110.

[17] Reddy, S.R., Sobieczky, H., Dulikravic, G.S. and Abdoli, A., 2016. Multi-element winglets: Multi-objective optimization of aerodynamic shapes. *Journal of Aircraft, 53*(4), pp.992-1000. doi:10.2514/1.C033334.

[18] Padmanathan, P. et al., 2024. Parametric optimization study of novel winglets for transonic aircraft wings. *Applied Sciences, 14*(17), p.7483. doi:10.3390/app14177483.

[19] Sethunathan, P., Ramasamy, K.K., Sivasubramaniyam, A.P. and Kannan, R., 2024. Aerodynamic performance of semi-wing with multiple winglets operating at low- and medium-range Reynolds numbers. *International Journal of Modern Physics C, 35*(10), p. 2450134.

[20] Bala, M.N.V.S.S., Kalali, S.K.G., Goud, B.N., Kumar, A.S. and Gupta, M.S., 2023. Flow investigation of a multiple winglet wing model. *AIP Conference Proceedings, 2492* (1), p.*020002.*

[21] El Haddad, N., 2015. Aerodynamic and structural design of a winglet for enhanced performance of a business jet. *Master's Thesis, Embry-Riddle Aeronautical University.*

[22] Lovegren, J. and Hansman, R.J., 2011. Estimation of potential aircraft fuel burn reduction in cruise via speed and altitude optimization strategies, *Master's Thesis*, Massachusetts Institute of Technology.

[23] Ulrich, L., Roche, L. and Consulting, L.R., 2001. Induced drag reduction with the WINGGRID device. *Aerodynamic Drag Reduction Technologies.* Berlin, Heidelberg: Springer Berlin Heidelberg, pp.304-311. doi:10.1007/978-3-540-45359-8_32.

[24] Ebrahimi, A. and Mardani, R., 2018. Tip-vortex noise reduction of a wind turbine using a winglet. *Journal of Energy Engineering, 144*(1), p. 04017052.

[25] Yin, K., 2017. A study of carbon dioxide emissions reduction opportunities for airlines on Australian international routes. *Master's Thesis*, The University of Queensland, Brisbane.

[26] Arifuzzaman, M. and Mashud, M., 2012. Design construction and performance test of a low-cost subsonic wind tunnel. *IOSR Journal of Engineering (IOSRJEN), 2*(10), pp.83-92.

[27] Rahman, M.M., Shayor, A.A., Al-Faruk, A. and Evan, M.T.R., 2025. Numerical investigation with experimental validation of aerodynamics performance of NACA 2414 airfoil with passive momentum injection through channeling. *Results in Engineering, 25*, p.104533.

[28] Berens, M., 2008. Potential of multi-winglet systems to improve aircraft performance, *Master's Thesis,* Technical University Berlin, Berlin.

This page is left intentionally blank

Journal of Engineering Advancements (JEA)

DOI: https://doi.org/10.38032/jea

Indexed by:

Volume 06 Issue 01

DOI: https://doi.org/10.38032/jea.2025.01

Published by: SciEn Publishing Group

Website: www.scienpg.com